Dynamic Rupture Scenarios of the Cascadia Megathrust based on Interseismic Locking Models

Yuk Po Bowie Chan[1], Suli Yao[1], Hongfeng Yang[1, 2]

[1]Earth and Environmental Sciences Programme, The Chinese University of Hong Kong, Hong Kong, China, [2]Shenzhen Research Institute, The Chinese University of Hong Kong, Shenzhen, China

Correspondence to:
H. Yang,
hyang@cuhk.edu.hk

Key Points:

- We conduct 3D dynamic rupture simulations for the future possible scenarios in Cascadia with constraints from interseismic locking models
- Application of different hypocenter locations reveals rupture segmentation and rupture directivity
- Our dynamic rupture scenarios have reasonably consistent segmentation extents and coastal subsidence patterns with paleoseismic observations

Abstract

The Cascadia subduction zone in the Pacific Northwest has well-documented geological records of megathrust earthquakes with the most recent Mw 9 rupture occurring in 1700 A.D. The paleoseismic observations suggest that Southern Cascadia is mature for future earthquakes since the last event. Consequently, it is crucial to investigate the potential rupture scenarios. Various interseismic locking models are developed along Cascadia, including offshore uncertainties and different material assumptions. Although they all share similar moment deficits, whether future earthquakes may rupture the entire margin or be segmented, as found in the paleoseismic records, remains unknown. Accordingly, we aim to investigate: (1) possible rupture segmentation patterns, (2) whether south Cascadia can host margin-wide ruptures, and (3) whether the existing locking models suggest similar future rupture scenarios. We estimate the stress distribution constrained by the locking models from static calculation and discover

that they lead to different stress distributions, indicating distinct seismic potentials despite their similar moment deficits. Our dynamic rupture scenarios show that the south can generate both segmented ruptures (> Mw 7.3 - 8.4) and margin-wide ruptures (> Mw 8.6) depending on hypocenter locations. The extent of Schmalzle-based segmented scenarios matches the proposed historical segmented events, and the margin-wide scenarios are well consistent with the coastal subsidence records of 1700 A.D. Therefore, we propose that three high-slip trench-breaching patches are sufficient for reproducing historical subsidence records. Our reasonable dynamic simulations can be applied in future studies for assessing seismic and tsunami hazards, and also serve as a comparison for non-trench-breaching scenarios.

Plain Language Summary

Earthquakes occur when the shear stresses on a fault overcome the frictional resistance to cause a sudden slip. In subduction zones, the tectonic plates converge and the stresses accumulate at the contact between the plates. As more stresses accumulate on the interface, great earthquakes are possible. Although there are no significant earthquakes (> Mw 8) since 1700 A.D., the Cascadia subduction zone in the Pacific Northwest is known to have historical Mw 9 earthquakes based on geological studies. Interseismic locking models describe the relative motion of the fault. For instance, 1 means fully locked where the two sides do not move against each other, thus accumulating stress. We infer stress distributions from interseismic locking models and conduct 3D dynamic simulations based on the stresses to explore possible future earthquake extents. Our results demonstrate various scenarios, including single-segment (> Mw 7.3 – 8.2), multiple-segments (> Mw 8.2 – 8.4), and full-margin ruptures (> Mw 8.6). Most of these scenarios are consistent with geological records, suggesting our scenarios are reasonable future earthquake estimates.

1. Introduction

The Cascadia subduction zone is known to host great megathrust earthquakes as large as moment magnitude (Mw) 9 (Wang and Tréhu, 2016; Walton et al., 2021). Based on paleoseismic records (Long and Shennan 1998; Kelsey et al. 2005; Goldfinger et al. 2012; Engelhart et al. 2015), the average recurrence interval of these events is about 500 yrs but with large variations. It has been over 322 years since the latest great earthquake, an M ~9 margin-wide rupture in A.D. 1700

accompanied with a large, trans-Pacific tsunami (Atwater and Hemphill-Haley 1997; Goldfinger et al. 2012, 2017; Satake et al., 2003). Modern interseismic geodetic observations indicate accumulation of energy along almost the entire Cascadia margin towards a future earthquake (Flück et al., 1997; Wang et al., 2003; Burgette et al., 2009; McCaffrey et al., 2013; Schmalzle et al. 2014; Pollitz and Evans, 2017; Li et al. 2018; Michel et al. 2019; Lindsey et al. 2021).

One challenge in seismic hazard assessment at Cascadia is estimating the potential of rupture segmentation along the megathrust. There are questions regarding whether past events were predominantly full-margin ruptures or sequences of smaller ruptures that were too closely spaced in time to be resolved by paleoseismic records (Wang et al., 2013; Atwater et al. 2014; Frankel et al. 2015). Along-strike heterogeneities in megathrust and crustal structure are thought to have the potential to cause rupture segmentation in various parts of the margin (Tréhu et al., 2012; Wang and Tréhu, 2016; Watt and Brothers, 2021). Based on the interpretation of offshore turbidity records, megathrust earthquakes occurred more frequently in southern Cascadia, especially south of Cape Blanco (Goldfinger et al., 2017). The average recurrence interval is inferred to increase from around 200 years in the south to around 300 years in the central segment and 400-500 years in the north (Witter et al., 2012; Goldfinger et al. 2017). If the A.D.1700 event was a full-margin rupture as inferred by Satake et al. (2003), then at present the short-recurrence southern segment is statistically expected to be more ready for the next rupture. The first scientific question we address in this study is whether the next large earthquake is more likely a full-margin rupture or to be confined in the south.

Dynamic rupture scenarios based on interseismic locking models can contribute to estimating the magnitude, rupture extent, and potential segmentation of future earthquakes (Yang et al., 2019a; Li and Liu, 2021; Ramos et al., 2021; Yao and Yang, 2022). For instance, Yang et al. (2019a) derived dynamic scenarios for the Costa Rica subduction zone by using interseismic locking models to derive the initial stress of the megathrust prior to the rupture and were able to explain the rupture extent and magnitude of the 2012 Nicoya Mw 7.6 earthquake. Using a similar approach, Ramos et al. (2021) conducted dynamic rupture simulations for Cascadia with the initial stress based on the interseismic locking model of Schmalzle et al. (2014). By nucleating ruptures from a high-stress location either in the south or in the north, they obtained scenarios of margin-wide rupture. Li and Liu (2021) conducted quasi-dynamic numerical simulation of long-term fault behavior in Cascadia. They inferred fault rate-state friction stability from

interseismic locking models (Schmalzle et al. 2014; Burgette et al., 2009). They found that whether the rupture was full-margin depended on what locking model was used.

Besides rupture extent and earthquake magnitude, the effect of rupture directivity on ground motion should be further investigated using dynamic rupture simulations. It is well understood that, with a heterogeneous initial stress distribution along the fault, different hypocenter locations can lead to different rupture directivities (Yang et al., 2019b; Yao and Yang, 2022). Even with a similar rupture extent, a different rupture directivity leads to a very different pattern of ground motion intensity (Yao and Yang, 2022). Therefore, the second scientific question we address in this study is how hypocenter location controls rupture directivity to impact ground motion.

To investigate the above questions, we carry out dynamic rupture simulation to obtain self-consistent rupture scenarios. We consider different Cascadia megathrust locking models (Figure 1), namely those by Schmalzle et al. (2014), Li et al. (2018), and Lindsey et al. (2021). Our research aims to derive rupture scenarios originating from South Cascadia. Assuming the same stress accumulation time, we investigate the role of stress distribution and hypocenter location in producing possible segmentation patterns and ground motion patterns. We further compare the rupture scenarios with the proposed segmented paleoearthquakes as well as coseismic subsidence amplitudes.

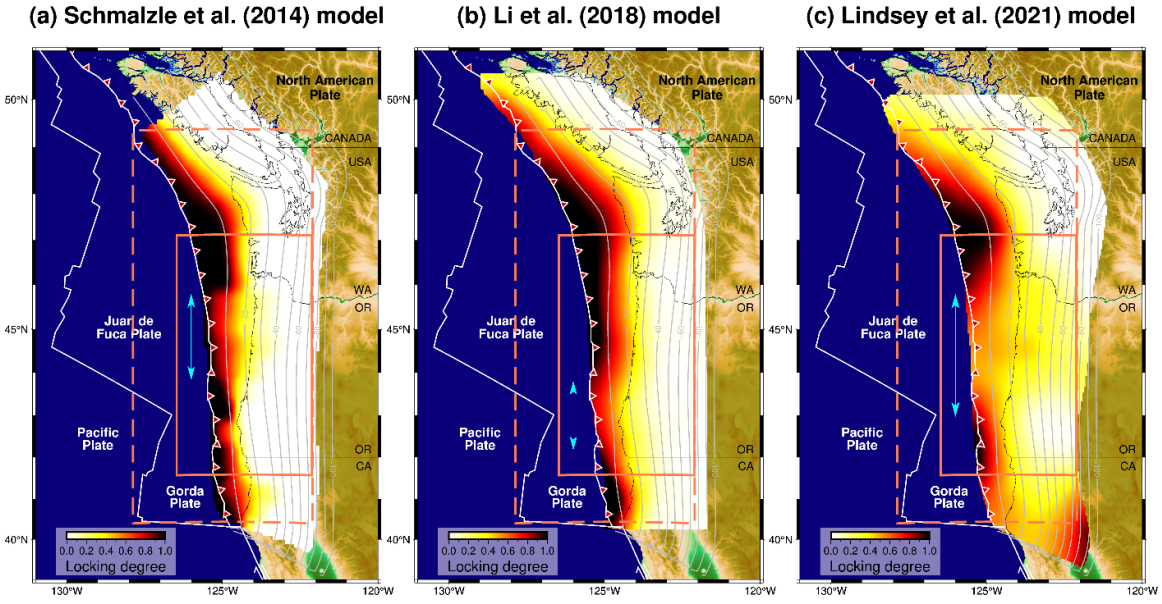

Figure 1. Interseismic locking models for CSZ. (a) Model from Schmalzle et al. (2014). (b) Model from Li et al. (2018). (c) Model from Lindsey et al. (2021). Coral dashed line: our static calculation domain. Coral solid line: our dynamic simulation domain. Cyan arrow: central creeping segments.

2. Interseismic locking models of the Cascadia megathrust

Since solutions for the inversion of geodetic measurements are nonunique, different assumptions are applied in deriving interseismic locking models, governing the smoothness of slip distribution and the degree of locking at the trench (McCaffrey et al., 2013; Schmalzle et al. 2014; Pollitz and Evans, 2017; Li et al. 2018; Michel et al. 2019; Lindsey et al. 2021). Here we summarize the three locking models adopted in this work, all derived by inverting land-based GNSS observations (Figure 1). Although Cascadia does not have a geomorphological trench because of the thick sediment cover, we refer to the deformation front as the "trench" in the following discussion for wording convenience.

Because land-based GNSS measurements cannot resolve the locking state of the shallowest portion of the megathrust which is far offshore, Schmalzle et al. (2014), following McCaffrey et al. (2013), proposed two models of opposite, prescribed near-trench locking states which fit the GNSS data equally well. One model assumes full locking at the trench with the locking degree monotonically decreasing downdip following the Gamma function designed by Wang et al. (2003) (Gamma model). The other model assumes a Gaussian-like locking distribution so that creeping occurs at the trench and full locking occurs farther downdip (Gaussian model). Creeping of the shallowest part of the fault may occur in a transient fashion such as during earthquake afterslip or slow slip events but is unlikely a sustained behavior over the interseismic period (Wang and Dixon, 2004; Wang, 2007). Thus, in this study we only use the Gamma model, referred to as the Schmalzle model hereafter (Figure 1a).

Following the explanation of Wang and Dixon (2004) and Wang (2007), Lindsey et al. (2021) included in their locking model the effect of stress shadowing in which a frictionally unlocked shallow segment of the fault may have little motion because of the neighboring frictionally locked patches immediately downdip. Although stress shadowing is explicitly invoked, the kinematic behavior of the megathrust in this model is similar to that described by the

aforementioned Gamma model. The difference in inversion results is caused mainly by assumed inversion parameters that constrain slip deficit distribution. In this study, we use their best-fit locking model, referred to as the Lindsey model (Figure 1c).

The above two locking models assume an elastic Earth, but the real Earth is viscoelastic, and viscoelastic stress relaxation plays an important role not only in postseismic but also interseismic deformation (Wang et al., 2012). To address this effect, Pollitz and Evans (2017) and Li et al. (2018) inverted Cascadia interseismic geodetic data based on analytical solutions and finite element models, respectively. Li et al. (2018) constructed many locking models that fit the geodetic data equally well. Here we only use their "preferred" locking model, referred to as the Li model (Figure 1b).

Because of the lack of near-field, seafloor geodetic constraints, all these models suffer from a high degree of nonuniqueness and thus contain large errors. By using these models to design initial fault stress distribution, we do not intend to construct a "correct" dynamic rupture model. Instead, we use these models to explore how different initial stress distributions may affect the rupture process. As such, these models may be considered as ad-hoc to each other. Improved understanding of the dynamic rupture process will help the design of kinematic rupture models for the purpose of probabilistic seismic hazard analyses and the appraisal of model uncertainties. We think the three models shown in Figure 1 adequately represent the range of assumptions used in constructing Cascadia megathrust locking models by different research groups in terms of Earth rheology, near-trench locking state, and smoothness of slip deficit distribution. Since stress accumulation is mostly determined by the spatial gradient of the locking distribution and the major first-order features of active faulting could be governed by the spatial gradients of stress (Nur, 1978), it is important to ask whether the slip deficit heterogeneities in these locking models can lead to consistent rupture scenarios.

3. Method and model parameter

We use open-source finite-element code PyLith which is developed for dynamic and quasi-static simulations of crustal deformation (Aagaard et al., 2017a). Input parameters for our dynamic simulation include fault geometry, material properties, initial stresses (τ_0), and fault frictional law parameters (Harris et al., 2018).

188

189 3.1 Megathrust geometry and mesh

190

191 We adopt the Cascadia megathrust model of McCrory et al. (2004), which has a smoothly
192 curved geometry starting from a 5 km depth below sea level and use an exponential curve to
193 approximate the shape of the upper plate near the trench as shown in Figure 2a.

194

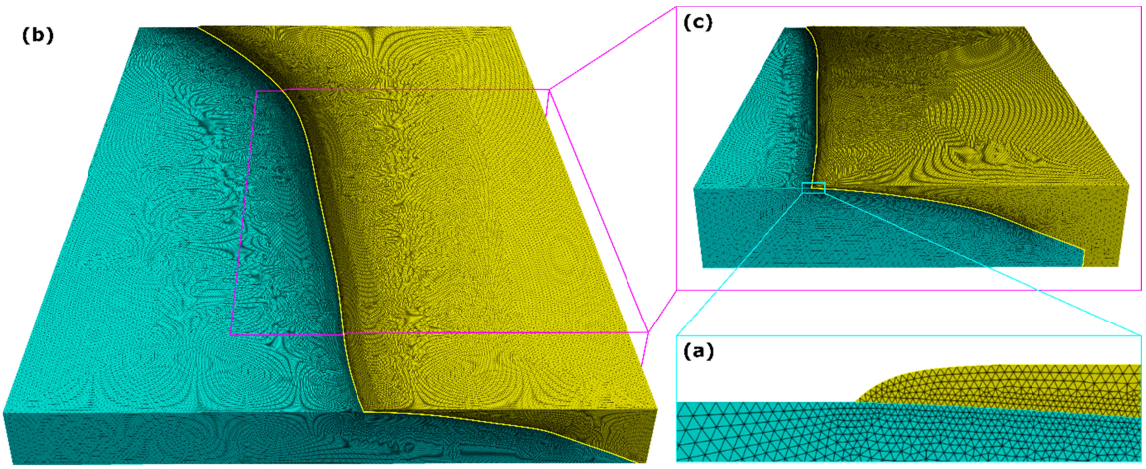

195

196 Figure 2. 3D model configuration. (a) Mesh geometry near the trench – continental block edge
197 approximated with an exponential curve away from the trench. (b) Finite element mesh for
198 static calculation with two model units: oceanic block (cyan) and continental block (yellow). (c)
199 Finite element for the dynamic simulations.

200

201 We generate two 3D tetrahedral meshes for Cascadia using geometry and mesh generation
202 software CUBIT (Blacker et al., 2016) to accommodate scientific purposes and computational
203 cost. Both meshes each consists of two model units - the oceanic block and the continental block.
204 We use the larger one of the two meshes, extending from 40.5°N to 49°N covering the whole
205 megathrust (Figure 2) to calculate stress distribution from locking models. We apply a
206 coordinate transformation to fix the origin at -129°E, 39°N. This larger mesh extends 970 km,
207 600 km, and 75 km in the strike, strike-normal, and depth dimensions, respectively (Figure 2b).
208 The element size on the fault is 500 m above 35 km depth for the major locked zone and
209 gradually increases downdip.

210

211 For computational efficiency, we use the smaller one of the two meshes, extending from
212 41.5°N to 47°N, to conduct dynamic rupture simulation in our area of focus. We are focused

mainly on the scenarios of rupture initiation in the south and on the effect of the central segment. Geological evidence of ruptures limited to northern Cascadia is elusive (Petersen et al. 2014), suggesting that ruptures breaking the northern segment might eventually develop into margin-wide ruptures. This is consistent with the higher stress accumulation in the north provided by most locking models (Burgette et al. 2009; McCaffrey et al. 2013; Schmalzle et al. 2014; Pollitz and Evans, 2017; Li et al. 2018; Michel et al. 2019; Lindsey et al. 2021) as well as the dynamic simulation results from Ramos et al. (2021). The small mesh covers the entire southern and central Cascadia, extending 600 km, 420 km, and 95 km in the strike, strike-normal, and depth dimensions, respectively (Figure 2c). The element size is 500 m above 50 km depth and gradually increases further downdip.

To minimize potential artefacts due to mesh boundaries, we extend the small mesh for the dynamic simulation to 95 km depth and even deeper than the larger mesh for static calculation by 20 km. In comparison, interseismic locking occurs mostly shallower than 30 km depth (Figure 1) and, to be further explained in sections 3.3 and 4.1, the model-predicted rupture propagation does not extend far beyond this depth because of lack of inferred interseismic stress built-up farther downdip. As will be shown section 4.2, none of our simulations features rupture deeper than 50 km depth.

3.2 Material Properties

Similar to most other dynamic rupture models, we assume an elastic Earth and apply absorbing conditions to all boundaries except the free surface at the top. The material property structure is based on the 3D Community Velocity Model (CVM) of Cascadia (Stephenson et al. 2017) in which the body wave velocities of the oceanic block are approximately 30% higher than the continental block. The density is calculated from p-wave velocity based on the empirical relationship of Brocher (2005). We have tested two different material property structures in order to see how they affect the dynamic rupture process. One model is referred to as the 1-D velocity model, in which the material properties of the continental block are applied to the whole mesh. Another model is referred to as the bi-material velocity model, where material properties of both continental and oceanic blocks are considered (Figure S1). The two structures lead to very similar rupture scenarios. Between the two test models shown in Figure S2, the moment

magnitude differs only by 0.01 (Figure S2). Hence, we use the 1-D velocity structure for the rest of our dynamic simulations (Figure 3a).

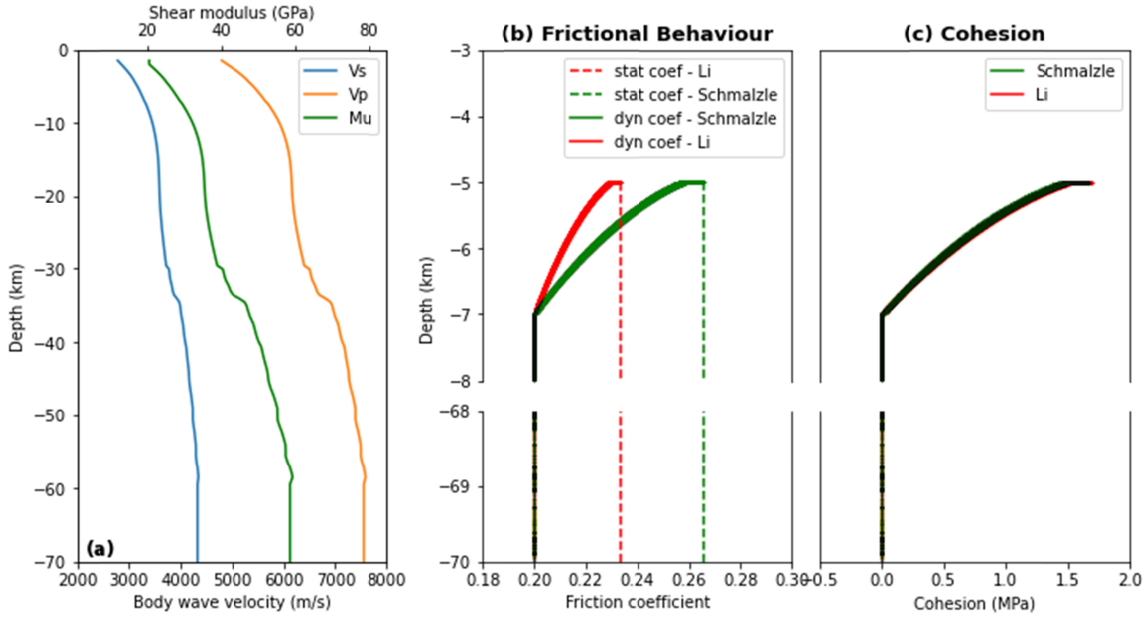

Figure 3. Depth-dependent parameters for dynamic rupture simulations. (a) 1-D velocity model calculated from Stephenson et al. (2017) and shear modulus. (b) Dynamic and static coefficients which remain constant below 7 km depth. (c) Cohesion, remaining constant below 7 km depth. Note that it appears dark because the two curves are overlapping.

3.3 Stress accumulation and initial stress on the megathrust

Following previous studies (Yang et al., 2019b; Ramos et al., 2021), we assume that the slip deficit has been continuously accumulated since the A.D.1700 earthquake. There are uncertainties associated with this assumption because there are no observational constraints on whether medium size earthquakes or significant creep occurred in the seismogenic depth range of the megathrust after 1700 but before the instrumental era. Upon interpreting GNSS velocity variations, Materna et al. (2019) proposed temporal variations in megathrust locking in southernmost Cascadia updip of the ETS zone associated with stress perturbations due to offshore M6+ earthquakes in the incoming oceanic plate. We do not include these complicated temporal variations in our calculation of slip deficit because neither the uniqueness of the GNSS data interpretation nor the physical mechanism of the proposed variations are well understood.

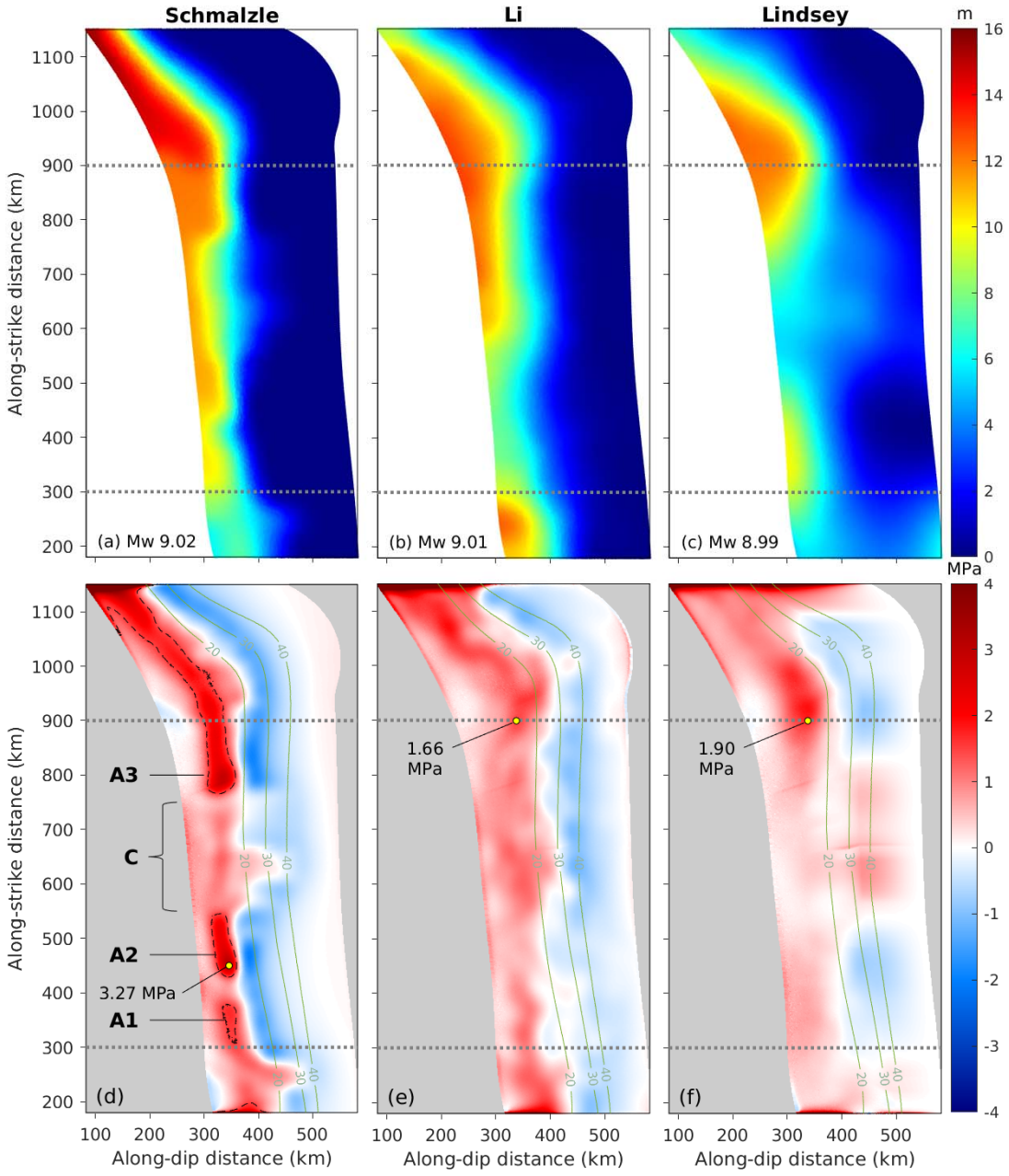

Figure 4. Slip deficit and stress change. (a) – (c): Total slip deficit with a uniform stress accumulation time of 320 years. Dotted lines: the boundaries of the dynamic simulation domain. (d) – (f): Dip component of the stress build-up caused by the slip deficit in (a) – (c). Dotted lines: the boundaries of the dynamic simulation domain. Yellow dots: the point of highest stress change magnitude within the dynamic modelling domain. Dashed lines in (d): 1.5 MPa stress contours. A1, A2, and A3 refer to the stress asperities while C marks the creeping segment extent.

With the interseismic locking distribution assumed to be time-independent, the slip deficit at present (Figures 5a – 5c) is simply the product of the subduction rate, slip deficit rate as a fraction of the subduction rate as given by the locking models (i.e., the locking degree in Figure 1), and the time since the A.D. 1700 great earthquake. In an elastic model, the incremental stress associated with the accumulation of this slip deficit can be readily determined from the slip deficit distribution (similar to the determination of static stress drop from coseismic slip distribution) (Figures 5d – 5f). Following Yang et al. (2019b) and Ramos et al. (2021), we assume that this incremental stress solely propels the next megathrust rupture (Figure 4), which implies that the "base level" of the fault stress plays no role, that is, whether the A.D.1700 event feature complete or partial stress drop is unimportant. It also means that the spatial heterogeneity of the fault stress distribution just after that earthquake is unimportant. This assumption is obviously a leap of faith, but it is theoretically consistent with the slip-weakening friction law invoked in our modelling which will be explained in section 3.4, and it makes it operationally possible to derive initial fault stress from interseismic locking models. Note that the incremental stress derived from one of locking models shown in Figures 1c and 5c occurs far deeper than the commonly assumed seismogenic depth limit of around 30 km in some areas along the margin (Figure 4f). To confine seismic rupture within a reasonable depth range, we use a cosine function to taper the fault stress in this model to zero from 35 km to 75 km depth (Figure 4f).

Effective normal stress is the normal stress minus pore fluid pressure. For simplicity, we assumed as a uniform effective normal stress of 50 MPa on the entire megathrust regardless of how the shear stress varies along the fault. This low effective normal stress is based on the notion of very high pore fluid pressurization at depths as inferred for global subduction zones (Saffer and Tobin, 2011). For example, given an average rock density 2500 kg/m^3, an effective normal stress 50 MPa at depth 20 km requires pore fluid pressure about 90% of the lithostatic pressure. There is no reason against other small values such as 30 or 60 MPa, and the lack of depth dependence is for the numerical convenience with little observational support. Nonetheless, the number 50 MPa we use is a typical value over the velocity-weakening region which is often used in earthquake simulation studies (Lapusta and Liu, 2009; Michel et al., 2017; Yang et al., 2019a).

309 Cascadia is well-known for Episodic Tremor and Slip (ETS) events (Rogers and Dragert, 2003).
310 Gao and Wang (2017) suggest that although the effective normal stress in the ETS region is
311 exceptionally low because of near-lithostatic fluid pressure, the ETS zone is rheological
312 separated from the seismogenic zone and thus is not involved in dynamic rupture. As will be
313 shown in section 4.2, in our models the rupture is arrested before reaching the ETS zone without
314 additional constraints, which is consistent with the notion of Gao and Wang (2017).
315

316 Based on findings of high-rate friction experiments (e.g., Di Toro et al., 2011), we set a dynamic
317 friction coefficient of 0.2 (i.e., dynamic stress level of 10 MPa) for the fault below 7 km and
318 assume it to be constant. The southern Cascadia material for the frontal thrust is
319 velocity-weakening while the northern Cascadia material is velocity-strengthening
320 (Stanislowski et al., 2022). For simplicity, we assume that the frontal thrust is neutrally stable by
321 increasing the dynamic coefficient linearly to the static coefficient levels of 0.2656 and 0.2332
322 for Schmalzle and Li models respectively (Figure 3b and Table 1) from 7 km updip to 5 km depth.
323 The initial stress prior to the dynamic rupture is the sum of the dynamic stress and the
324 interseismic stress accumulation inferred from the locking models.

325

326 ***Table 1*** *Model parameters in dynamic rupture simulations*

Fault parameter	Schmalzle model	Li model
Static friction coefficient, f_s (yield strength/σ_n)	0.2656	0.2332
Dynamic friction coefficient, f_d (dynamic stress/σ_n)	0.2	0.2
Effective normal stress, σ_n (MPa)	50	50
Critical weakening distance (m)	0.6, 1	0.6, 1

327

328 3.4 Fault frictional law and resolution test

329

330 The fault is assumed to be governed by the linear slip-weakening law (Ida, 1972) in which fault
331 shear stress τ_f is given by (Aagaard et al., 2017b),

$$\tau_f = \begin{cases} \tau_c - (\mu_s - (\mu_s - \mu_d)\frac{d}{d_c})\tau_n & d \le d_c \; and \; \tau_n \le 0 \\ \tau_c - \mu_d \tau_n & d > d_c \; and \; \tau_n \le 0 \\ 0 & \tau_n > 0 \end{cases} \quad (1)$$

where μ_s is the static friction coefficient, μ_d is the dynamic friction coefficient, d_c is the slip-weakening distance, τ_n is the effective normal stress, τ_c is the cohesive stress, and d is the slip distance. The frictional resistance (τ_f) decreases linearly with increasing fault slip when $d < d_c$ but stays constant when $d > d_c$. It is should be emphasize that, according to the slip-weakening law, the rupture behavior is controlled by the difference between yield stress and initial stress instead of the absolute stress level.

We set the yield stress, which is the product of static friction coefficient and normal stress, to be uniformly 0.01 MPa above the maximum initial shear stress on the fault within the dynamic modelling domain (Figure 3b and Table 1). For example, the highest interseismic stress accumulation within the region of dynamic modelling in accordance with the Schmalzle slip deficit distribution is 3.27 MPa (Figure 4e) which, with the uniform dynamic stress 10 MPa, gives the highest initial stress 3.27 + 10 MPa = 13.27 MPa. The yield stress of the model based on the Schmalzle slip is thus l3.28 MPa, which translates to a static friction coefficient of 13.18/50 = 0.2656 (Table 1). The assumed homogeneity of the yield stress can be understood as an indication of relatively smooth megathrusts that are conducive to very large earthquakes, and its low amplitude reflects the low fault strength as inferred from heat flow data (Gao and Wang, 2014).

The highly compliant, frontal region of the accretionary prism could significantly impact the rupture scenarios as its inelastic deformation can act as an energy sink (Galvez et al., 2014). We tested the sensitivity of the assumed depth limit to the weak frontal prism. We found that strong free-surface reflections and amplified fault slip would be generated to facilitate trench-breaching rupture if a thinner frontal prism was used, but rupture would be halted if a thicker frontal prism was used (Figure S3). For simplicity, we adopt an average depth range (i.e. 5 – 7 km) for the frontal prism according to the velocity model of Stephenson et al. (2017) (Figure S4). Similar to Ramos et al. (2021), we add cohesion to the segment of the megathrust overlying the assumed frontal prism (Figure 3c) to suppress undesired rupture initiation near the trench.

Based on seismic observations, the critical weakening distance, d_c, has been suggested to be proportional to the local total slip, indicating spatially heterogeneous d_c on faults (Mikumo et al., 2003; Tinti et al. 2005; Fukuyama and Mikumo, 2007). However, because the slip distribution is now known a priori for future earthquakes, and the scaling relationship between slip and d_c has large uncertainties (Guatteri and Spudich, 2000; Chen and Yang, 2020), there is little information about d_c. Ensuring fair comparison among locking models is another challenge in deciding on d_c because the same d_c represents different fracture energy given the different initial stress and yield stress in each model. Dynamic models constructed by Weng and Yang (2018) and Yao and Yang (2020) show that a uniform d_c yields synthetic waveforms that compare with observations very well, and that a heterogeneous slip-scaled d_c does not lead to appreciable improvements. Therefore, we take the simpler approach of assuming a uniform d_c. We recognize the large uncertainties associated with the choice of d_c and test a range of uniform d_c values to see how the results are affected. In section 4.3, we will discuss the results using d_c of 1 m and 0.6 m.

Our models need to meet the resolution requirement. A cohesive zone refers to the fault plane portion behind the crack tip where shear stresses drop from static to dynamic value with a slip less than d_c (Ida 1972). The cohesive zone of in-plane (mode II) ruptures can be estimated by the following equation (Day et al., 2005)

$$\Lambda = \Lambda_0 A^{-1}(v), \qquad \Lambda_0 = \frac{9\pi}{32}\frac{\mu}{1-\nu}\frac{d_c}{\tau_s-\tau_d}, \tag{2}$$

where μ is shear modulus, ν is Poisson's ratio, and τ_s and τ_d are yield stress and dynamic shear stress, respectively. Considering d_c of 0.6 m - 1 m, the static cohesive zone sizes are around 7.5 - 25 km. Given a lower bound for shear wave speed Vs of 3.165 km/s and a rupture speed of 3.1 km/s, $A_{III}^{-1} = (1 - V_r^2/V_S^2)^{1/2} = 0.2$, the dynamic cohesive size can be as small as ~1.5 km. Aagaard et al. (2013) demonstrate that PyLith can resolve cohesive zones around 1.5 times the size of the tetrahedral elements. Therefore, our element size of 500 m on the fault can resolve cohesive zones in our models.

3.5 Rupture initiation

The nucleation zone refers to the area where the rupture begins. In the prescribed nucleation zone, the initial stress has to meet the yield stress to initiate the rupture. To initiate a rupture, we decrease the yield strength inside the designated nucleation zone by decreasing the static friction coefficient within the nucleation zone from the τ_s values shown in Table 1 to $\tau_s^i =$

0.2001. In order to initiate a spontaneous rupture, a nucleation zone needs to exceed a critical size (Yang et al., 2019a),

$$A_1 = \frac{(3\pi)^3}{2^{11}} \frac{\overline{\tau_0 - \tau_d}}{\tau_s - \tau_s^i} \frac{(\tau_s - \tau_d)^2}{(\overline{\tau_0 - \tau_d})^4} \mu^2 d_c^2 . \quad (3)$$

So $\overline{\tau_0 - \tau_d}$ and $(\tau_s - \tau_s^i)$ denote average static stress drop and strength decrease within the nucleation zone respectively. For instance, given an average static stress drop of 1.5 MPa and d_c of 0.6 m for the Schmalzle model, the critical radius of a circular nucleation zone is 13.6 km.

We tested nucleation zone radii of 10 km and 15 km, comparable with those adopted in dynamic modeling studies for the 2011 M9.1 Tohoku earthquake (Duan 2012; Ide and Aochi 2012; Galvez et al. 2014). With different nucleation sizes, the model-predicted rupture scenarios for the same hypocenter locations are similar (Figure S5). To ensure that our rupture scenarios could represent first-order features from the interseismic locking models instead of the interpolation methods, the nucleation zone size has to be comparable to the patch size or node spacing used during inversion (Figure 5), especially for the Li model. Thus, we adopted a larger radius of 15 km. We then conduct simulations on ten along-strike hypocenter locations in southern Cascadia spanning from 41.77° - 44.47° latitude. A range of depths is also tested depending on the positive stress change distribution of each locking model.

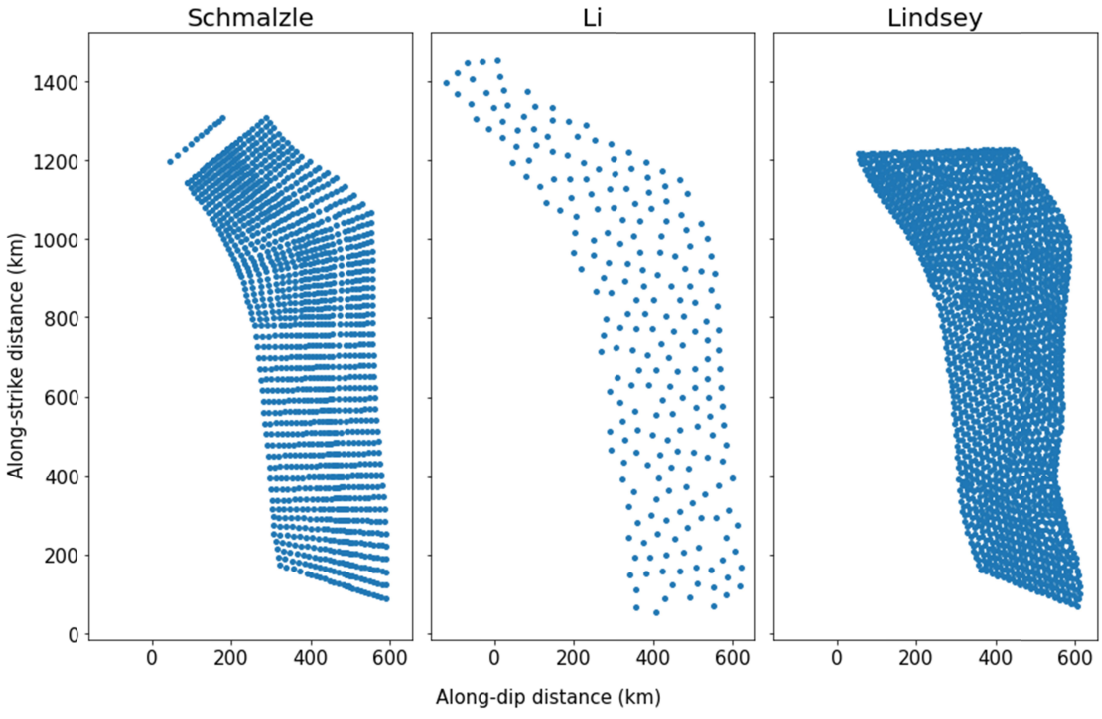

414 Figure 5. Spatial distribution of original data points for the three interseismic locking models.
415
416 4. Results
417
418 4.1 Stress build-up from locking distribution
419
420 From static calculations as described in section 3.3, we obtain distributions of stress
421 accumulation from the total slip deficit (Figure 4). Since the stress change along strike is
422 negligibly small, only the dip component is shown in Figure 4d – 5f. Nevertheless, the strike
423 component is used in our dynamic simulations and the points of the highest stress change are
424 determined by the magnitude of stress change vectors. The slip deficit distributions calculated
425 from the locking models have similar patterns and their moment magnitude within the static
426 model domain only differs by 0.03 (i.e. Mw 8.99-9.02) (Figure 4). All of the three locking
427 models feature high slip deficit above 12 m in northern Cascadia (above 900 km along-strike
428 distance in Figure 4). The largest contrast between the models is in the south and central
429 segments. For example, the segment that exhibits more creep is located at 550-750 km, 300-550
430 km, and 500-700 km in the Schmalzle, Li, and Lindsey models, respectively, with different
431 maximum slip deficits (Figures 5a – 5c). The derived stress accumulation distributions display a
432 larger difference in along-strike variations among these models (Figures 5d – 5f).
433
434 The depth extent of positive stress build-up based on the Schmalzle model extends to ~20 km
435 depth. We can locate three high-stress patches, labelled A1, A2, and A3 in Figure 4d in our
436 dynamic model domain. A2 hosts the maximum stress build-up of 3.3 MPa. Between the A2 and
437 A3, there is a creeping segment with obviously lower stress (labeled C in Figure 4d). Such stark
438 along-strike variations are not that obvious in the slip deficit distribution (Figure 4a), because the
439 stress accumulation is proportional to the second derivative of slip deficit. While A2 and A3
440 host sharp downdip decrease in slip deficit within a narrow locking zone, the C segment has a
441 more gradual decrease with deeper locking depths. This illustrates that the stress distributions
442 can reveal the seismic potentials that may not be identified as first-order features in slip deficit
443 distributions.
444
445 The stress build-up based on the Li model shows a more uniform along-strike distribution,
446 except in the northernmost region where the highest slip deficit takes place (Figure 4). The

positive stress in this model extends deeper, to ~30 km depth. Although it has a longer zone of low slip deficit than in the Schmalzle model, there are no distinct high-stress patches but only a slightly low-stress patch at 400-500 km (Figure 4e). The maximum accumulated stress in the dynamic model domain is only 1.7 MPa.

The Lindsey model shows a somewhat similar along-strike variation of stress distribution to the Schmalzle model even though the amplitude is different (Figure 4). The slip deficit amplitude of the Lindsey model is significantly lower than the Schmalzle model, having maximum accumulated stress of 1.9 MPa in the north. Yet, their spatial gradient variations along strike are alike. The south and the north have steeper slip deficit gradients constrained in shallower depths ~30 km while the creeping segment has a noticeable gentle decrease in slip deficit until the slab bottom (Figure 4c). Considering that rupture segmentation is dominated by the spatial variation of stress instead of the amplitude, we expect results akin to the Schmalzle model given modifications of frictional parameters regarding the amplitude. Because of the poorly constrained down-dip locking depths, the Lindsey stress model is not further evaluated for dynamic simulations.

4.2 Predicted rupture scenarios

Using the initial stress which includes accumulated stress derived from locking models, we initiate the ruptures with a range of hypocenter locations. In some dynamic scenarios, the ruptures propagate outside with considerable rupture extent, classified as breakaway scenarios. The examples of breakaway scenarios using d_c of 0.6 m and 1 m are shown in Figure 6-7 and Figure S6 respectively. While in other cases, the rupture propagation stops immediately outside the nucleation zones due to the lack of elastic energy release to overcome the fracture energy required to weaken the fault, termed self-arresting events (Figure 8). The moment magnitude for scenarios is calculated according to the integral of the final slip (d) over the fault plane area (A) using an average shear modulus (μ) of 35 GPa ($M_0=\mu Ad$; $Mw=2/3*(\log_{10}(M_0) - 9.1)$). Our moment magnitude gives a lower limit for the scenarios that propagate out of the model domain (e.g. Figure 6e & 6g). The slip rate means the relative particle velocity across the fault while the rupture speed is the rate of rupture front movement (Rowe and Griffith, 2015), calculated every 10 seconds.

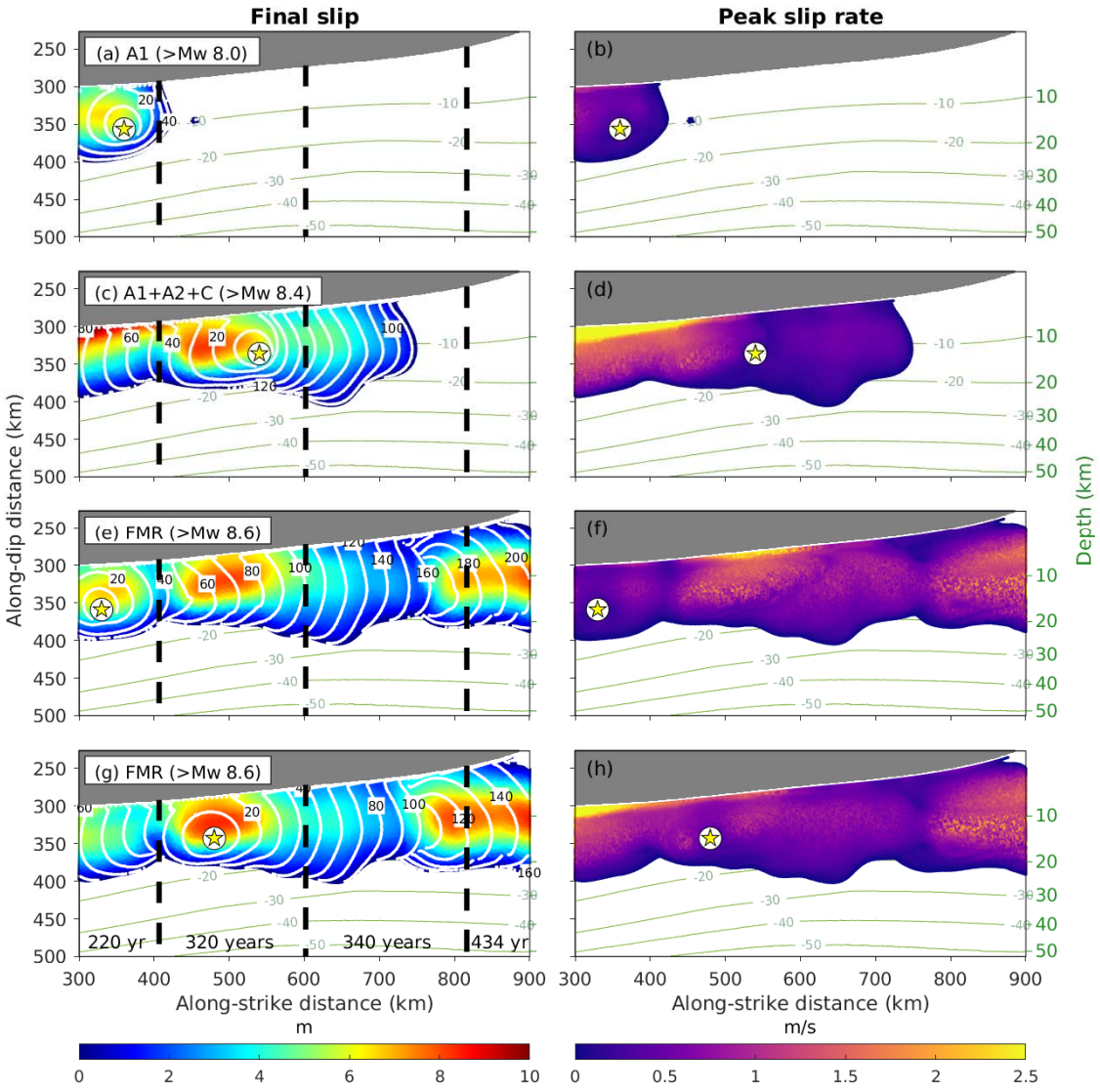

Figure 6. Dynamic rupture scenarios derived from the stress distribution of the Schmalzle model using a dc of 0.6 m. (a), (c), (e), (g): Final slip distribution. Stars: hypocenter locations. Olive-green contours: slab depth contours. Rupture fronts (white contours) are displayed every 10 seconds and numbered every 20 seconds. Black dashed lines: recurrence time intervals of 220, 320, 340, and 434 years (Goldfinger et al., 2017) as written in (g). The labeled Mw is calculated by slip within the model domain, thus scenarios with slip extending outside the domain should have larger magnitudes. (b), (d), (f), (h): Peak slip rate throughout the rupture. Stars: hypocenter locations. Olive-green contours: slab depth contours. (a) – (b): Scenario rupturing the A1 asperity. (c) – (d): Scenario rupturing A1 and A2 asperities and part of the creeping segment C. (e) – (f): Full-margin rupture (FMR) initiated from A1. (g) – (h): Full-margin rupture initiated from A2.

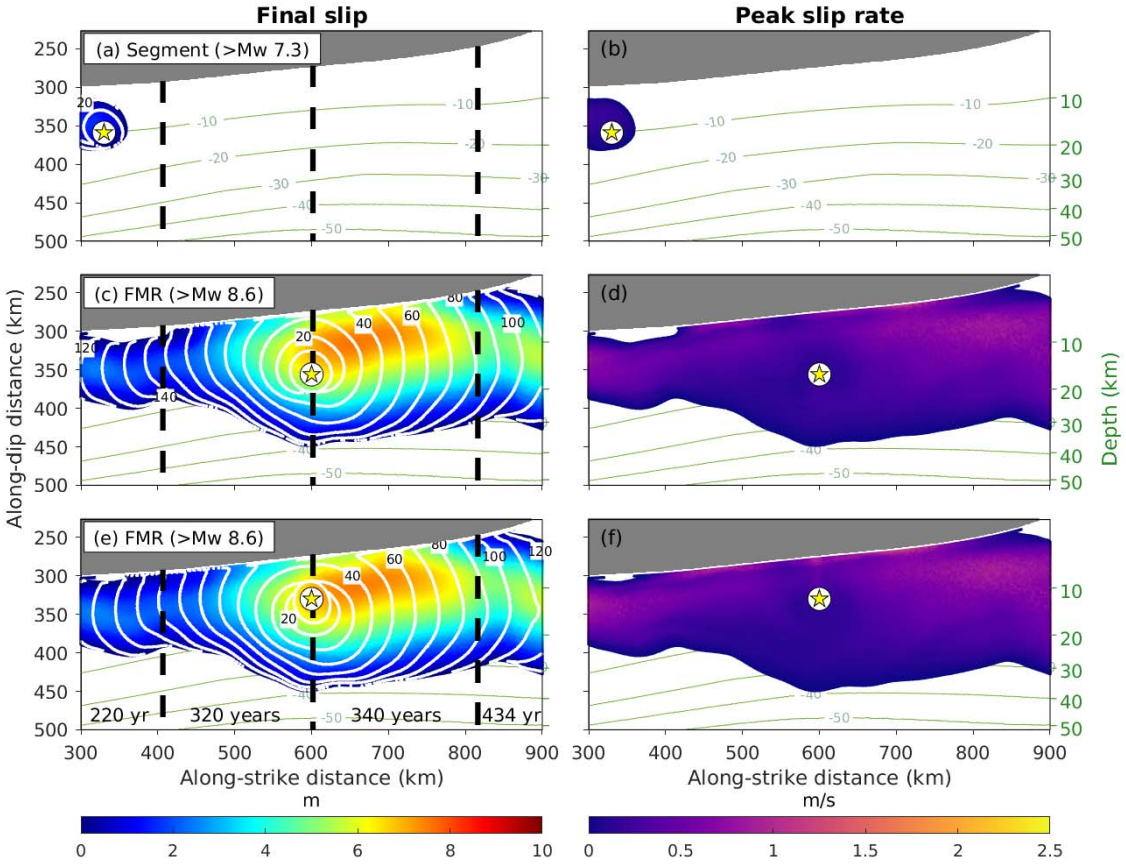

Figure 7. Dynamic rupture scenarios derived from the stress distribution of the Li model using a dc of 0.6 m. Same as Figure 6, except for the Li model. (a) – (b): Segmented rupture scenario. (c) – (f): FMR for different hypocenter locations.

We further classify the self-arresting and breakaway events explicitly. According to the empirical relationships between the rupture area and magnitude, the rupture within the nucleation zone is around Mw 6.5 (Wells and Coppersmith, 1994). Earthquakes generally have rupture velocities higher than 1 km/s (Rowe and Griffith, 2015) and demonstrate a ratio between rupture velocity and v_s starting from around 0.4 (Weng and Ampuero, 2020). Since our v_s at trench (5 km depth) is 3.17 km/s, we expect breakaway ruptures to reach rupture velocities higher than 1.27 km/s (0.4 v_s). Consequently, we define the scenarios with Mw < 6.5 and rupture speed less than 1.27 km/s as self-arresting ruptures, and those above as breakaway ruptures. Our analysis will only focus on the breakaway ruptures, considering self-arresting ruptures are merely the results of artificial nucleation.

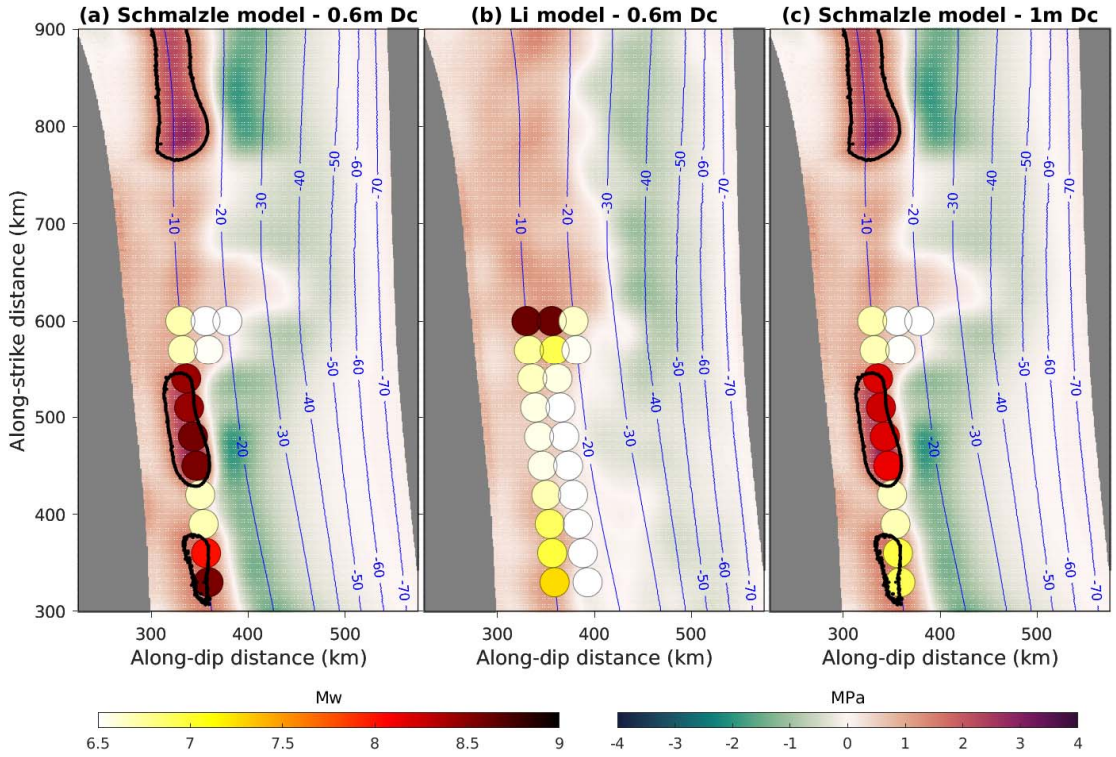

Figure 8. Moment magnitude dependence on hypocenter locations. Map view of the moment magnitudes of rupture scenarios nucleated at each location (circles) with the stress build-up in the background, and slab depth contours (blue lines). (a) Scenarios derived from the Schmalzle model using a dc of 0.6 m. Black lines: 1.5 MPa stress contour, same as in Figure 4. (b) Scenarios acquired from the Li model using a dc of 0.6 m. (c) Same as (a) except for a dc of 1 m (Figure S6).

We further divide the breakaway ruptures into segmented ruptures and full-margin ruptures. "Full-margin ruptures" represent rupture scenarios that propagate out of the entire model domain. Because the northern Cascadia holds the highest accumulated stress and our model domain includes a part of the northern segment, it is reasonable to assume that the ruptures propagating out of the domain's northern boundary would eventually rupture the entire northern Cascadia. Similarly, the southern segment inside the domain has consistent stress levels with the southernmost Cascadia outside of the domain, hence we assume the "full-margin ruptures" can break the southern Cascadia as well. For this reason, we name the ruptures propagating out of the south and north of the domain as "full-margin ruptures" in the

following context. In contrast, the scenarios where their along-strike rupture extents within the model domain are regarded as segmented ruptures.

Full-margin ruptures are shown in both the Schmalzle-based (Figure 6e-h) and the Li-based scenarios (Figure 7c-f) with maximum final slips of 8.5 m and 7.6 m respectively. Those of the Schmalzle model are larger than Mw 8.6, reaching a rupture speed of 3.1 km/s and a peak slip rate of 4.5 m/s. The source durations last for more than 150-200 seconds depending on the hypocentre location (Figure 9a). On the other hand, the moment magnitudes of full margin ruptures from the Li model are also higher than Mw 8.6. They have a slightly lower rupture velocity of 2.7 km/s and a peak slip rate of 1.4 m/s. The source duration is less than 140 seconds (Figure 9a). The full-margin ruptures of the Schmalzle model and the Li model halted at 30 km and 40 km depths respectively. All are initially predominated by crack-like ruptures, evolving into pulse-like ruptures (Movies S1-S4).

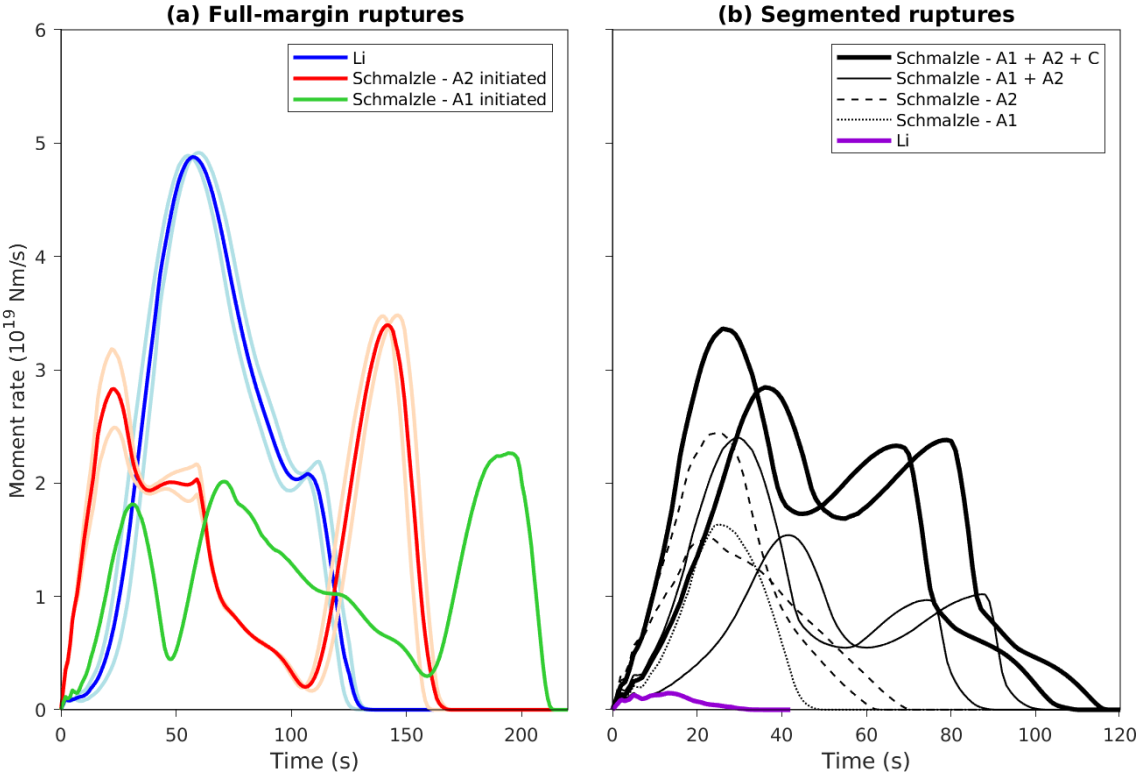

Figure 9. Moment rate functions from dynamic rupture simulations. (a) Moment rate of all full-margin rupture scenarios. Moment rate functions of individual neighboring rupture scenarios are indicated by lighter colors (light blue for the Li model and pink for those initiated from A2 in the Schmalzle model) and the average is marked by solid colors (blue for the Li

model and red for the A2 initiation in the Schmalzle model). Note that there is only one event initiated from A2 in the Schmalzle model (green line). (b) Moment rate of all segmented ruptures for the Schmalzle model (black lines) and Li model (purple line). A1 and A1+A2+C ruptures were derived using a dc of 0.6 m while A2 and A1+A2 scenarios were simulated with a dc of 1 m (Figure S6). The only segmented event from the Li model utilizes a dc of 0.6 m.

Despite having the same accretionary wedge setting as in Figure S4b, all the scenarios shown here, except case 6c, do not demonstrate the large near-trench slip as tested above because of the different hypocenter locations and stress distribution. For the Schmalzle model, as the rupture initiates in the south, the combined effects from rupture directivity and free surface reflection in the south are smaller as compared to initiation from the north. As for the case of 6c, its hypocenter is located further north, thus allowing a stronger directivity. However, such high slip trench features are also absent in the north even with hypocenters in the south. This is because while the rupture propagates through the central creeping segment, the energy depletes and it is insufficient to cause a large slip until it reaches the high-stress asperity at the north. For the Li model, the high-slip trench is also absent because there are no particular high-stress asperities that could trigger larger slip near the trench.

Rupture segmentation is observed in both models. From the Schmalzle model dynamic scenarios, we observed one scenario breaking A1 (Figure 6a) and two scenarios rupturing A1, A2, and partly C (Figure 6c). The A1 segmented rupture (Figure 6a) is initiated by a hypocenter location at A1 asperity and the source duration continues for 40 seconds (Figure 9b), with rupture stopped above 20 km depth. Both A1+A2+C scenarios (Figure 6c) are triggered by nucleation at A2 asperity, and the source durations last for 110-120 seconds (Figure 9b), having slip above 30 km depth. For the Li model, only one dynamic segmented scenario is found rupturing the southernmost segment. Since the rupture initiation is close to the domain boundary, the rupture propagates out of the south quickly after nucleation while being arrested in the north and above 20 km depth (Figure 7a), resulting in a duration time as short as 30 seconds (Figure 9b). Except for the A1+A2+C dynamic models which have similar rupture evolution behaviors to the full-margin ruptures (Movie S5), the short segment ruptures (Figure 6a and 7a) are primarily crack-like ruptures as the rupture duration is insufficient for them to grow into pulses (Movies S6-7).

579 4.3 Hypocentral effects on the potential moment magnitude and ground surface response
580
581 In view of the different resulting scenarios, we investigate the effect of different hypocenters in
582 both models with a d_c of 0.6 m. For the heterogeneous Schmalzle model, there is a strong
583 along-strike variation in moment magnitude with respect to the stress distribution (Figure 8a).
584 The nucleation zones within the highest stress patch A2 result in scenarios with Mw > 8.4-8.6
585 and the events within A1 have Mw >8.0-8.6. All the nucleation centers lying outside of the stress
586 asperity results in self-arresting ruptures. This demonstrates the hypocentral dependency of
587 magnitudes in the Schmalzle model.
588
589 Meanwhile, the Li geodetic locking model gives a smoother and more homogeneous stress
590 distribution within the model domain that does not flavor rupture segmentation except in the
591 southernmost region where the initial stress is slightly higher (Figure 8b). Although full-margin
592 ruptures take place with hypocenters in a particular region, it by no means suggests that the
593 ruptures are larger on that site. It shows that the initiation of full-margin ruptures is sensitive to
594 slight stress perturbations on the fault. Recalling our assumptions of linear stress accumulation
595 and uniform background stress level, small deviations on these assumptions (e.g., spatial
596 variations in stress accumulation time and material properties) could cause comparable stress
597 distribution perturbations in the Li model while the perturbations would be relatively
598 insignificant in the Schmalzle model. Thus, the Schmalzle model shows clearer seismic
599 potential while the Li model is more ambiguous considering the uncertainties in stress
600 accumulation evolution and background stress field.
601
602 Apart from the moment magnitude, the hypocentral effects on ground surface response are also
603 noticeable. We compare the velocity magnitude of synthetic stations near major cities derived
604 from the margin-wide scenarios in both models (Figure 10). Although the rupture extent from
605 the scenarios of different hypocentres in each model is highly similar (Figure 10a), the
606 amplitude of peak ground velocity can differ twice. For instance, in the Li model, the two
607 hypocenters have the same along-strike distance but different downdip depths - 10 km and 15 km.
608 The deeper nucleation event (15 km) clearly demonstrates larger peak ground velocities than the
609 shallower one (10 km) at stations CAVE, DBO, BUCK, and LOKI. Such a difference is
610 primarily due to the rupture propagation. For the 15 km event, the rupture propagates updip since
611 initiation, setting off a strong wavefront (Figure 7c). However, the 10 km event starts by

propagating downdip and is followed by updip fault slip along the sides of the nucleation zone, creating two wavefronts shortly after the nucleation (Figure 7e). The interference of these seismic waves and those from downdip fault slip leads to a more ambiguous waveform slightly lagging behind the 15 km event even though the 10 km one is in closer proximity to the surface.

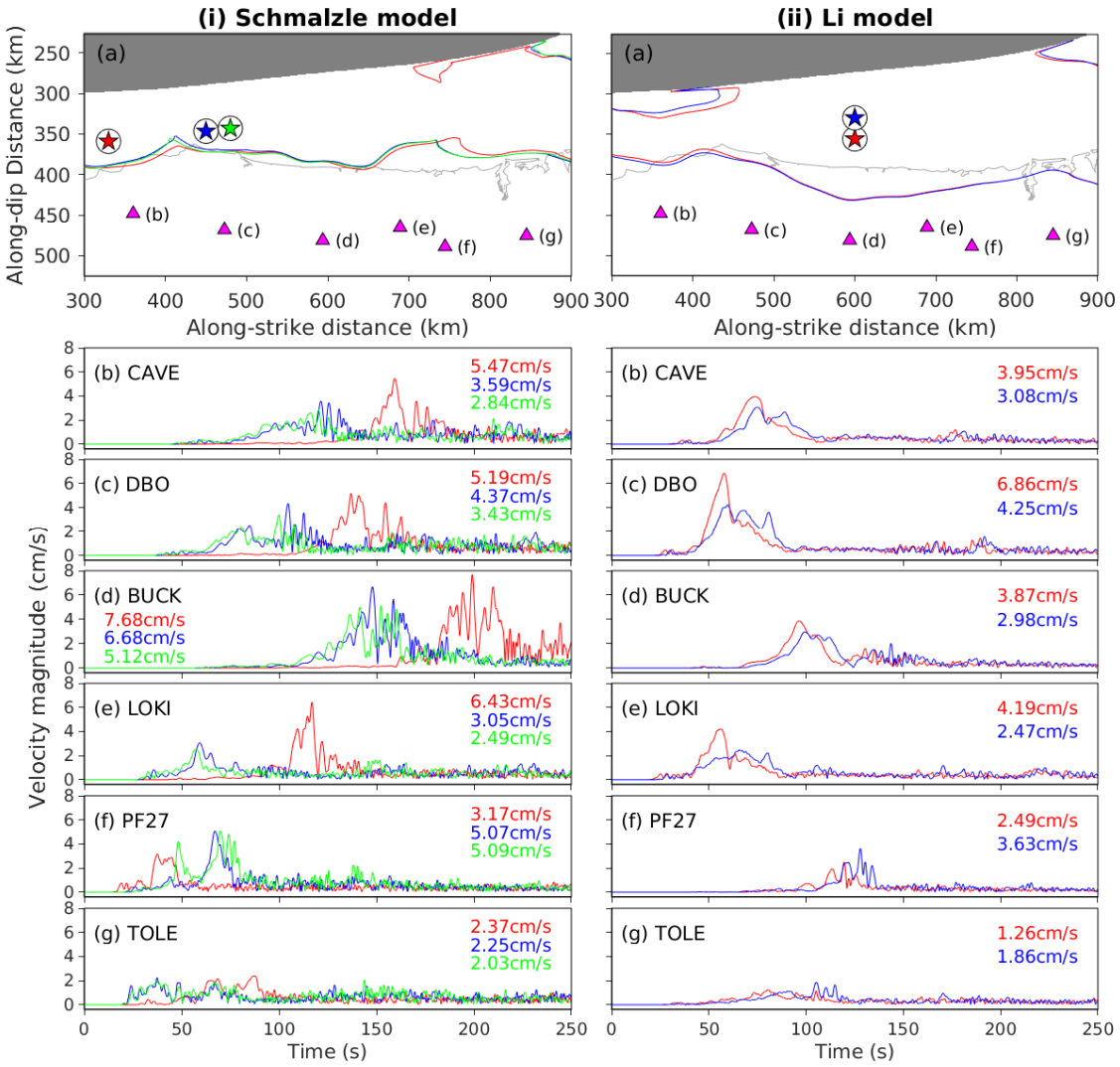

Figure 10. Synthetic velocity magnitude at stations for FMR. (a) The 1 m final slip contour of rupture scenarios with the coastline (light grey). The colors of the slip contours match with the star (hypocenter location) colors. Magenta triangles: station locations. Labels beside stations: the plot number. The stations near major cities along the strike are selected from the Pacific Northwest Seismic Network. (b) – (g) Comparison of velocity magnitudes (three-component combined) among the rupture scenarios in (a) with matching colors. The corresponding peak velocity magnitudes and station names are marked on each trace. (i) Schmalzle model. (ii) Li model.

The hypocentre at a different location along-strike also results in different waveforms. In the Schmalzle model, there are two hypocentres in A2 and one hypocentre in A1 contributing to margin-wide ruptures. Since the A1 hypocentre event propagates from the southernmost region to the north of the domain, the strong directivity causes a distinct pulse as compared to the A2 hypocentre events. For example, the LOKI station has peak velocity magnitudes of 2.5-3 cm/s for the A2 hypocentres but 6.4 cm/s for the A1 hypocentre (Figure 10ei).

4.4 Seafloor deformation and coastal subsidence in margin-wide scenarios

We also evaluate the surface deformation patterns for our margin-wide rupture scenarios. The peak vertical ground displacements for the Schmalzle-based and Li-based scenarios are similar in magnitude, ranging from -1.1 m to +1.0 m and from -1.2 m to +1.1 m respectively. On the other hand, the maximum peak ground velocity of the Schmalzle-based scenarios (i.e. 2.3 m/s) is remarkably higher than that of the Li-based scenarios (i.e. 1.2 m/s) by almost double. Both models show the highest peak ground velocity towards the tip of the continental crust and the northernmost region of the domain.

Coseismic hingeline refers to the point where there is zero seafloor vertical displacement. Compared to the Schmalzle model (Figure 11b), the coseismic hingeline for the Li model (Figure 11d) is further inland, especially for the central and northern segments because the down-dip rupture extent of these regions in the Li's model is deeper (Ramos et al., 2021). However, it is noted that the down-dip locking depth of the seismogenic zone is poorly constrained by geodetic data (Wang and Tréhu, 2016), thus we only focus on the along-strike variations of coastal subsidence instead of the absolute amplitudes.

The average coastal subsidence is then extracted from the peak vertical ground displacement of the data points closest to the coastline in all the margin-wide scenarios in both models (Figure 11a). We then compare the synthetics with the subsidence records of the A.D. 1700 M9 earthquake. In our scenarios, Li's coastal subsidence gives a more distinct pattern compared to the observations, having the largest amount of deformation at the high slip patch in the north and decreasing further away. For scenarios from Schmalzle model, the along-strike coseismic subsidence appears to fluctuate with slightly larger deformation in high-slip segments region.

659 The subsidence records of the A.D.1700 M9 rupture also exhibit heterogeneous along-strike
660 pattern, which can be matched by models with several high slip patches (Wang et al., 2013). In
661 our case, the scenarios from Schmalzle model can reproduce a similar along-strike variation
662 with the observations, mainly due to the higher slip heterogeneity with three high-slip patches
663 (Figure 6) compared to those from Li model (Figure 7).
664

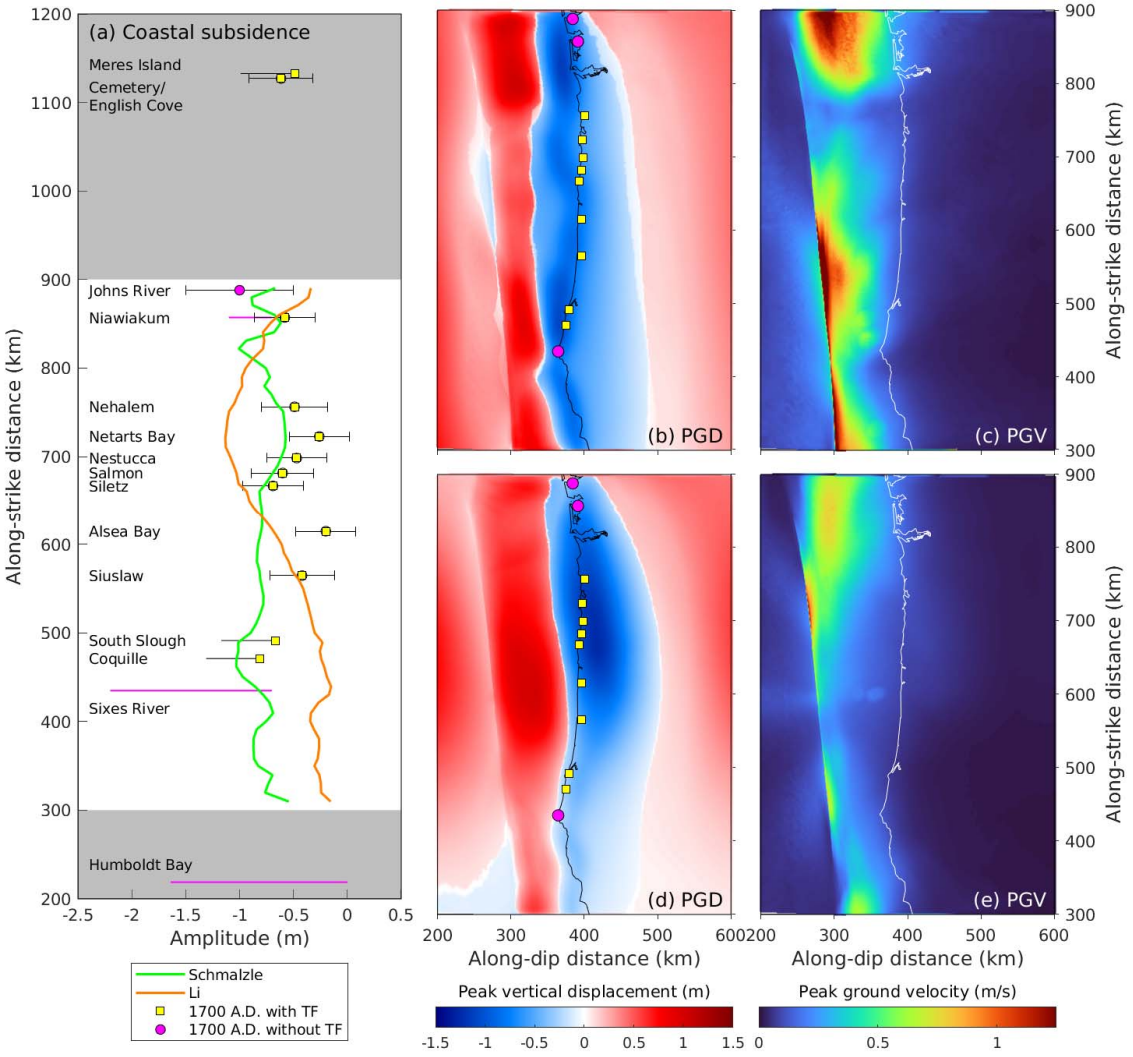

665

666 Figure 11. Ground motion intensities of full-margin ruptures. (a) Average peak vertical ground
667 displacement along the coastline for the Schmalzle model (green line) and the Li model
668 (orange line). Yellow squares: observations sites with transfer function analysis (TF). Pink
669 circles: sites without TF. Error bars: one standard deviation. Black lines with yellow squares at
670 one end: yellow squares as the minimum estimates. Pink line: uniform distribution. Grey
671 patches: regions outside of the model domain. (b) Peak vertical ground displacement of
672 full-margin ruptures in Schmalzle model with the coastline (black line). Observation sites with

673 (yellow square) and without (pink circles) TF analysis (Wang et al., 2013). (c) Average peak
674 ground velocity PGV of FMR derived in the Schmalzle model with the coastline (white line).
675 (d) – (e): Same as (b) and (c) respectively except for the Li model.
676
677 5. Discussions
678
679 5.1 Potential rupture patterns in correlation with recorded segmentation and recurrence
680 intervals
681
682 The rupture extents of segmented scenarios in the Schmalzle model are consistent with the
683 recorded segmentation of paleoearthquakes (Goldfinger, 2012, 2017). The A1 scenario arrested
684 around the 220-320 years recurrence interval boundary (Figure 6a), and all cases for A2 and
685 A1+A2 ruptures stopped around the 320-340 years boundary as it enters the creeping segment
686 (Figure S6). For A1+A2+C cases, the ruptures extend to part of the 340-year recurrence interval
687 segment but not the whole (Figure 6c). This is because the A3 asperity is located slightly off the
688 recurrence interval boundary. Therefore, the ruptures could either arrest before A3 or propagates
689 to the rest of the high-stress northern region, causing full-margin ruptures. There are also
690 ambiguities in determining the paleoseismic rupture limits due to limitations in core data. Hence,
691 the A1+A2+C scenario is supported by the estimated minimum rupture limit in the segmented
692 rupture model (Goldfinger et al., 2017) where rupture stops before the 340-year segment. On the
693 other hand, the Li model does not share particular similarities with the recurrence interval
694 segments within the model domain.
695
696 We also find that the margin-wide ruptures can be derived for all models given certain
697 frictional parameters. Given the 320 years of silence and the recurrence intervals of 220-340
698 years in the south, all segmented scenarios are possible in the current stage. Although there are
699 few constraints on the frictional parameters of the Cascadia megathrust, our combination of
700 parameters allows variations in rupture scenarios, including segmented and margin-wide
701 ruptures comparable with the geological records. This may suggest that the ratio between the
702 frictional parameters and initial stresses is reasonable, if not the absolute amplitudes. The
703 margin-wide rupture initiates at A1 and A2 in the Schmalzle model and the boundary between
704 320 and 340 recurrence intervals for the Li model. This reflects that at the current state, the

705 possibility of ruptures initiating from the south or central Cascadia growing into a margin-wide
706 rupture cannot be eliminated.
707
708 The diverse segmentation in our scenarios results from heterogeneous locking and various
709 hypocentre locations. Ramos et al. (2021) initiated dynamic rupture simulations at locations of
710 highest stress drop in the south, resulting in full-margin ruptures for scenarios with uniform
711 stress accumulation time, and both full-margin and segmented rupture scenarios using
712 heterogeneous stress accumulation time along strike which is determined empirically. Indeed,
713 the uncertainties in the stress accumulation history could be introduced by a heterogeneous
714 time interval. However, with strong along-strike differences in accumulation time, the stress
715 distribution becomes largely affected by the empirical time interval instead of the locking
716 distribution. Our study shows that segmented ruptures are possible even using a uniform stress
717 accumulation time when different nucleation zones are used. The application of hypocentre
718 locations discovers the possibilities of rupture initiation from a range of stress drops, thus more
719 segmentation patterns are found apart from the largest possible margin-wide ruptures (Figure
720 12).
721

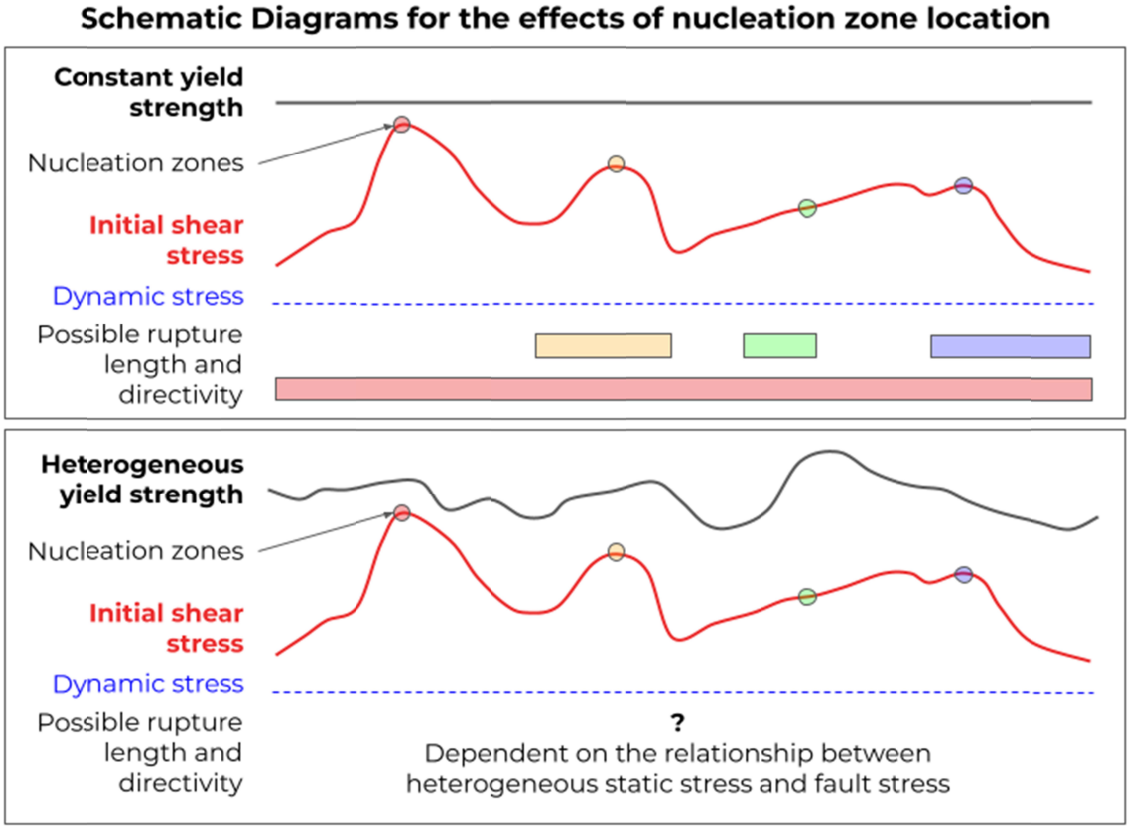

722

723 Figure 12. A schematic diagram demonstrating the potential rupture segmentation by applying
724 different hypocenter locations.
725
726 5.2 Simulated coseismic subsidence compared with A.D. 1700 records
727
728 Although the along-strike variation of the heterogeneous Schmalzle-based coastal subsidence
729 has a reasonable consistency with the paleoseismic records, our synthetic subsidence is
730 generally slightly larger than the observations, exceeding one standard deviation in two sites
731 (i.e., Alsea Bay and Siuslaw) at the central segment. Here we will provide possible reasons for
732 such discrepancy.
733
734 Similar to the earthquake sequence simulations (Li and Liu, 2021), our subsidence is larger
735 than the observational data at Alsea Bay. Our research focuses on estimating future
736 earthquakes thus we assume homogenous background stress levels immediately after the A.D.
737 1700 margin-wide rupture. However, the background for A.D. 1700 could in fact be
738 heterogeneous due to the spatial and temporal uncertainties in the geodetic locking and the slip
739 history before the A.D. 1700 rupture. It is possible to reconstruct best-fit subsidence results by
740 adjusting accumulation time empirically as in Ramos et al. (2021) but this is beyond the scope
741 of our study.
742
743 Another important factor controlling subsidence is the inelastic accretionary prism deformation.
744 One outstanding example is the 2011 Tohoku-Oki earthquake where the region of the largest
745 slip does not cause the largest tsunami height possibly due to the inelastic deformation of the
746 accretionary prism (Fujiwara et al. 2017; Wilson and Ma, 2021). Han et al. (2017) observed an
747 along-strike variation for the consolidation state of the accreted sediments in Cascadia and
748 propose that this could contribute to the megathrust slip behavior. For instance, offshore
749 Washington has over-consolidated sediments incorporated into the mechanically strong outer
750 wedge, and very little sediment is being subducted, flavoring potential near-trench rupture. On
751 the other hand, a thick sequence of under-consolidated fluid-rich sediment is subducting
752 offshore Central Oregon, possibly facilitating elevated pore pressure, thus promoting possible
753 aseismic slip in this area. These factors may account for the slight deviation of our model
754 subsidence from the data.
755

5.3 Comparison between dynamic simulations and static methods

Our dynamic simulation showcases a lower moment release in all rupture scenarios than estimations from variant static methods. Static methods commonly provide the upper bound of possible slip by assuming complete release of slip deficit in future earthquakes (Figure 13). The maximum slip deficits within the model domain for both models only differ slightly – 12.9 m for the Schmalzle model and 13.0 m for the Li model. Consequently, the maximum slip in the Schmalzle-based dynamic rupture model (8.5 m) contributes about 66% of the maximum slip deficit, and that of the Li model (7.6 m) is about 59%. This difference with the static locking models is observed in a number of studies, including the potential rupture segmentations for the Anninghe fault in west China (Yao and Yang, 2022), the central American subduction zone where the 2012 Nicoya Mw 7.6 earthquake occurred (Yang et al., 2019a), Himalaya front where the 2015 Nepal Mw 7.8 earthquake took place (Li et al., 2016), as well as the south American subduction zone where the 2010 Maule Mw 8.8 earthquake occurred (Moreno et al., 2010).

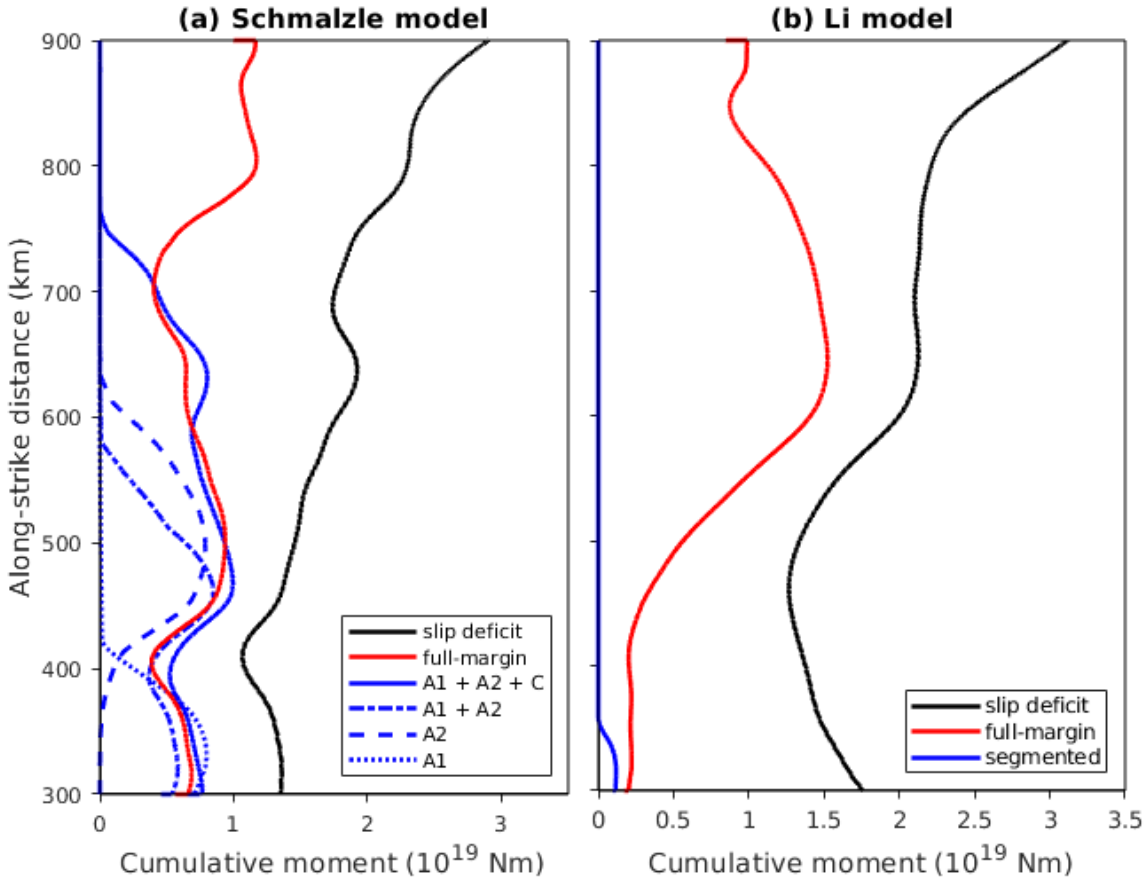

773 Figure 13. Cumulative moment versus the along-strike distance. The cumulative moment is the
774 product of rigidity, slip, and area, integrated over every 500m width along strike. Blue lines:
775 average cumulative moment for the segmented scenarios. Red lines: average cumulative
776 moment for full-margin ruptures. Black lines: cumulative moment assuming all slip deficit in
777 Figure 4 are released, also known as the moment deficit (Maurer et al. 2017). (a) Dominant
778 dynamic rupture scenario types and slip deficit for the Schmalzle model. (b) Same as (a) except
779 for the Li model.
780
781 These suggest that given our current frictional parameters, a considerable fraction of the slip
782 deficit in regions of low to moderate stress drop is not released during dynamic simulations in
783 our models (Figure 14 and 15). The stresses on these areas can be relieved later possibly in
784 form of coseismic events and slow slip events. For instance, Cascadia is well-known for its
785 episodic tremor and slow slip events. In addition, considering the poorly constrained downdip
786 limit of the seismogenic zone using geodetic observations, the unreleased slip deficit may in
787 fact represent uncertainties, including the portion for interseismic stress relaxation and the
788 temporal variation in locking width (Wang and Tréhu, 2016). Therefore, the discrepancy
789 highlights the necessity of conducting dynamic simulations on top of static calculations.
790

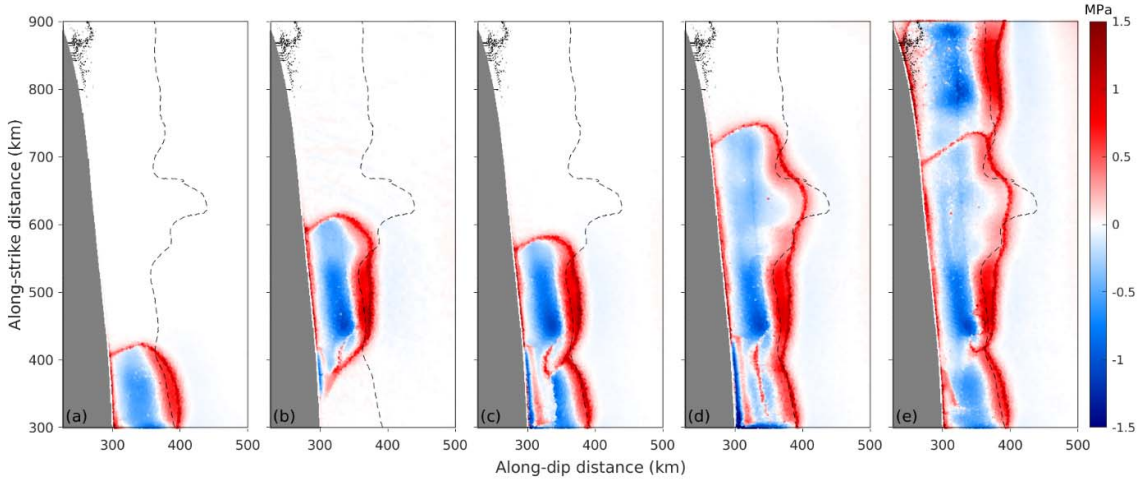

791
792 Figure 14. Stress change distributions for the Schmalzle -based rupture scenarios. Dashed lines:
793 contours of zero stress change derived from locking models (Figure 4). The up-dip portion of
794 the contour contains positive stress build-up. (a) Example of A1 rupture (Figure 6a). (b)
795 Example of A2 rupture (Figure S6c). (c) Example of A1+A2 rupture (Figure S6e). (d) Example
796 of A1+A2+C rupture (Figure 6c). (e) Example of a full-margin rupture (Figure 6g).
797

798 We further compared our results with the heterogeneous ruptures inferred from coastal
799 subsidence estimates. Wang et al. (2013) proposed a range of heterogeneous slip models for the
800 A.D. 1700 event using a 3D elastic dislocation model with reference to the subsidence
801 estimates. Assuming the fault slip patches follow the bell-shaped function, they adjusted the
802 slip patches parameters (e.g., size, location, and peak slip) to match the model-predicted
803 surface deformation to the paleoseismic subsidence estimates using a trial-and-error approach.
804 In particular, they preferred a model consisting of four high-slip patches for simplicity and
805 having a reasonable fit with the observations. However, the models are limited by the large
806 subsidence data gaps in northern and southern Cascadia (Figure 11).
807

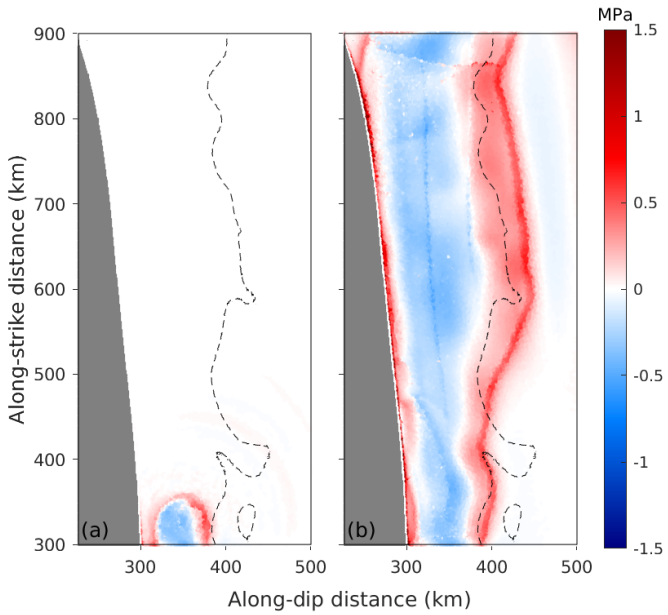

808
809 Figure 15. Stress change distributions for the Li-based rupture scenarios. (a) Example of
810 segmented rupture (Figure 7a). (b) Example of a full-margin rupture (Figure 7e).
811
812 In comparison, our scenarios incorporate the locking models utilizing Global Navigation
813 Satellite System GNSS data, which are more densely spaced along Cascadia, as the physical
814 constraints on rupture depth and heterogeneities. We demonstrate that three high-slip patches
815 in a dynamic rupture model could be sufficient to generate subsidence amplitudes similar to the
816 observation of the A.D. 1700 megathrust earthquake. Similarly, the Schmalzle
817 locking-constrained earthquake sequence simulation (Li and Liu, 2021) also suggests a three
818 high-slip patches scenario, and its synthetic subsidence is in good agreement with the

observational data. Therefore, the three high-slip patches scenarios could be close to the A.D.1700 event.

5.4 Limitations in deriving future coseismic slip

Although our dynamic models produce reasonable ground motions that match with multiple observational studies, there are limitations in constraining the up-dip frictional properties and rupture behaviors. The first concern comes from the frictional behaviors of the frontal prism. In our model, the strength drop (difference between static and dynamic stress) at the frontal prism decreases towards the trench, and the initial stress equals the addition of dynamic stress and stress drop from static simulation. Although cohesion could suppress fault failure at the beginning of the simulations, the stress perturbations from ruptures could induce higher slip rates at shallow depths as it easily overcomes the small strength drop, especially with the dynamic effects of free-surface reflection. However, in reality, velocity-strengthening materials are known to slip at low rates. Our models do not consider the plastic deformation of the frontal prism either. Indeed, cohesion could partly describe the energy absorption close to the free surface caused by the presence of unconsolidated gouge and clays (Galvez et al., 2014). However, the amplitude of cohesion in our case is not constrained by laboratory experiments, including local mineralogy, lithology, and fluid pressure. Moreover, the frictional behaviors in our model are prescribed for the fault interface and off-fault plasticity is neglected. Ulrich et al. (2022) and Wilson and Ma (2021) highlight the inelastic deformation of sediments as one of the dominant factors controlling seafloor deformation, hence tsunamic genesis. Incorporating off-fault plasticity and careful descriptions of frictional behaviors with respect to laboratory experiments and offshore geological studies would help establish realistic dynamic rupture scenarios.

Another major concern in estimating tsunami hazards comes from the uncertainty in future shallow rupture behavior. In our model, we assumed a simplified fault geometry where the fault extends to the top of the model domain, introducing trench-breaching ruptures in our dynamic models. Nevertheless, other rupture modes such as buried rupture, splay-faulting, and activation of thrusts and back-thrusts are possible (Wang and Tréhu, 2016). Gao et al. (2018) constructed hypothetical splay-fault geometries in addition to Priest et al. (2009) and a continuous along-strike frontal thrust model based on seismic profiles. Therefore, a more

detailed 3D mapping of the complex fault geometry could help evaluate the possibility of different rupture mechanisms using dynamic rupture simulations.

6. Conclusion

In this study, we conducted 3D dynamic rupture simulations for Cascadia using different interseismic locking models with a range of hypocenter locations in the South. While the locking models have similar static moments and locking distributions, their heterogeneous stress distribution leads to distinct rupture scenarios. Both Schmalzle and Li models demonstrate that the south is capable of generating Mw >8 segmented ruptures and full-margin ruptures depending on the frictional parameters and hypocenter locations. For instance, both segmented and full-margin ruptures can occur with the same hypocenter location given different frictional parameters.

We found that the heterogeneity of interseismic locking models plays a key role in determining the rupture process. The more heterogeneous Schmalzle locking model yields a stress distribution with more asperities, thus facilitating segmented ruptures on the high-stress asperities. These segmented ruptures appear to have a reasonable correlation with the along-strike extent of the inferred recurrence intervals. On the other hand, the more homogeneous Li locking model gives a smoother stress distribution, hence the scenarios are either full-margin ruptures or self- arrested ruptures. The selection of hypocenter location is also a crucial parameter in controlling the potential segmentation patterns. For the more heterogeneous model, the scenarios that initiated from the higher stress asperities demonstrate a significantly larger moment magnitude.

Accordingly, surface deformation is also largely controlled by these factors. While the homogeneous locking model results in a simpler coastal subsidence pattern with the largest subsidence in the region of highest slip and decreasing further away, the heterogeneous model gives a more complex pattern depending on the stress asperities. This also suggests that the A.D.1700 earthquake may represent a possibly more heterogeneous slip model provided its fluctuating coastal subsidence pattern. In particular, our results show that a three high-slip patches scenario can reproduce a reasonably similar seafloor deformation with the A.D. 1700 earthquake. Apart from coastal subsidence, the synthetic ground shaking also demonstrates that

rupture directivity is strongly controlled by prescribed hypocenter locations, leading to nearly double the peak ground velocity for scenarios initiated at different hypocenter locations even though the resulting slip distributions are almost the same.

This project can be further developed from multiple perspectives in the future, including the off-fault plasticity, the along-strike changes in accretionary prism geometry, and the addition of splay faults. Our simulation results can also be applied to tsunami modeling to evaluate the tsunami risks for each segmented rupture type. Furthermore, our models may help evaluate the present probabilistic seismic hazard analysis (PSHA) by providing possible slip distributions of the paleoearthquakes for source characterization as well as the synthetic ground motions for comparison with that generated by the empirical ground motion prediction equations.

On top of specific investigations on Cascadia, our findings could help understand the general relationship between interseismic locking models and the possible earthquake slip patterns, thus the moment magnitudes. Our study together with the dynamic simulations for the other fault zones, such as the Nicoya Peninsula subduction megathrust (Yang et al., 2019a) and the Anninghe fault (Yao and Yang, 2022), raises the possibility to provide new insights into more efficient slip estimations of seismic potentials for the fault zones worldwide in the future.

Data Availability Statement

All the data used in this work have been previously published, and references are provided in the paper. Dynamic rupture simulations were generated using the open-source software package PyLith, freely available at https://github.com/geodynamics/pylith. Locking model data may be found in the cited papers. All the important scripts and outputs are accessible in the temporal link https://drive.google.com/drive/folders/1sGSr1tuyvgm_kHL9mslxsHzwlLw3L2XX?usp=sharing during peer review. Upon acceptance of the manuscript, the data would be available in the CUHK Research Data Repository.

Acknowledgments

We greatly appreciate Kelin Wang and Yajing Liu for their constructive comments on this study. Financial support is provided by the National Key R&D Program of China (2018YFC1503400), Hong Kong Research Grant Council Grants (14306119, 14306418), China Earthquake Science Experiment Project, CEA (grant no. 2018CSES0102), State Key Lab of Earthquake Dynamics (grant No. LED2021B03), The Open Foundation of the United Laboratory of Numerical Earthquake Forecasting (grant No. 2021LNEF02), CUHK Direct Grant from Faculty of Science.

7. References

Aagaard, B. T., Knepley, M. G., & Williams, C. A. (2013). A domain decomposition approach to implementing fault slip in finite-element models of quasi-static and dynamic crustal deformation. *Journal of Geophysical Research: Solid Earth*, *118*(6), 3059-3079. https://doi.org/10.1002/jgrb.50217

Aagaard, B., M. Knepley, C. Williams (2017a), PyLith v2.2.1 [software]. Davis, CA: Computational Infrastructure of Geodynamics. DOI: 10.5281/zenodo.886600, url: https://geodynamics.org

Aagaard, B., M. Knepley, C. Williams (2017b), PyLith Manual, Version 2.2.1, Computational Infrastructure for Geodynamics, Davis, CA, url: https://geodynamics.org/resources/pylith/supportingdocs

Atwater, B. F., & Hemphill-Haley, E. (1997). *Recurrence intervals for great earthquakes of the past 3,500 years at northeastern Willapa Bay, Washington* (No. 1576). US Government Printing Office. https://doi.org/10.3133/pp1576

Atwater, B. F., Carson, B., Griggs, G. B., Johnson, H. P., & Salmi, M. S. (2014). Rethinking turbidite paleoseismology along the Cascadia subduction zone. *Geology*, *42*(9), 827-830. https://doi.org/10.1130/G35902.1

Blacker, T. D., Owen, S. J., Staten, M. L., Quadros, W. R., Hanks, B., Clark, B. W., Meyers, R.J., Ernst, C., Merkley, K., Morris, R., McBride, C., Stimpson, C. J., Plooster, M., & Showman, S. (2016). *CUBIT geometry and mesh generation toolkit 15.1 user*

945 *documentation* (No. SAND-2016-1649R) [software]. Sandia National Lab.(SNL-NM),
946 Albuquerque, NM (United States). https://doi.org/10.2172/1430472

947 Brocher, T. M. (2005). Empirical relations between elastic wavespeeds and density in the Earth's
948 crust. *Bulletin of the seismological Society of America*, *95*(6), 2081-2092.
949 https://doi.org/10.1785/0120050077

950 Burgette, R. J., Weldon, R. J., & Schmidt, D. A. (2009). Interseismic uplift rates for western
951 Oregon and along-strike variation in locking on the Cascadia subduction zone. *Journal of*
952 *Geophysical Research: Solid Earth*, *114*(B1). https://doi.org/10.1029/2008JB005679

953 Chen, X., & Yang, H. (2020). Effects of seismogenic width and low-velocity zones on
954 estimating slip-weakening distance from near-fault ground deformation. *Geophysical Journal*
955 *International*, *223*(3), 1497-1510. https://doi.org/10.1093/gji/ggaa385

956 Day, S. M., Dalguer, L. A., Lapusta, N., & Liu, Y. (2005). Comparison of finite difference and
957 boundary integral solutions to three-dimensional spontaneous rupture. *Journal of Geophysical*
958 *Research: Solid Earth*, *110*(B12). https://doi.org/10.1029/2005JB003813

959 Di Toro, G., Han, R., Hirose, T., De Paola, N., Nielsen, S., Mizoguchi, K., Ferri, F., Cocco, M.,
960 and Shimamoto, T. (2011). Fault lubrication during earthquakes. *Nature*, *471*(7339), 494-498.
961 https://doi.org/10.1038/nature09838

962 Duan, B. (2012). Dynamic rupture of the 2011 Mw 9.0 Tohoku-Oki earthquake: Roles of a
963 possible subducting seamount. *Journal of Geophysical Research: Solid Earth*, *117*(B5).
964 https://doi.org/10.1029/2011JB009124

965 Engelhart, S. E., Vacchi, M., Horton, B. P., Nelson, A. R., & Kopp, R. E. (2015). A sea-level
966 database for the Pacific coast of central North America. *Quaternary Science Reviews*, *113*, 78-92.
967 https://doi.org/10.1016/j.quascirev.2014.12.001

968 Flück, P., Hyndman, R. D., & Wang, K. (1997). Three-dimensional dislocation model for great
969 earthquakes of the Cascadia subduction zone. *Journal of Geophysical Research: Solid*
970 *Earth*, *102*(B9), 20539-20550. https://doi.org/10.1029/97JB01642

971 Frankel, A., Chen, R., Petersen, M., Moschetti, M., & Sherrod, B. (2015). 2014 update of the
972 Pacific Northwest portion of the US National Seismic Hazard Maps. *Earthquake Spectra*,
973 *31*(1_suppl), S131-S148. https://doi.org/10.1193/111314EQS193M

974 Fujiwara, T., dos Santos Ferreira, C., Bachmann, A. K., Strasser, M., Wefer, G., Sun, T.,
975 Kanamatsu, T., & Kodaira, S. (2017). Seafloor displacement after the 2011 Tohoku-Oki
976 earthquake in the northern Japan trench examined by repeated bathymetric
977 surveys. *Geophysical Research Letters*, *44*(23), 11-833.
978 https://doi.org/10.1002/2017GL075839

979 Fukuyama, E., & Mikumo, T. (2007). Slip-weakening distance estimated at near-fault
980 stations. *Geophysical research letters*, *34*(9). https://doi.org/10.1029/2006GL029203

981 Galvez, P., Ampuero, J. P., Dalguer, L. A., Somala, S. N., & Nissen-Meyer, T. (2014).
982 Dynamic earthquake rupture modelled with an unstructured 3-D spectral element method
983 applied to the 2011 M 9 Tohoku earthquake. *Geophysical Journal International*, *198*(2),
984 1222-1240. https://doi.org/10.1093/gji/ggu203

985 Gao, D., Wang, K., Insua, T. L., Sypus, M., Riedel, M., & Sun, T. (2018). Defining megathrust
986 tsunami source scenarios for northernmost Cascadia. *Natural Hazards*, *94*(1), 445-469.
987 https://doi.org/10.1007/s11069-018-3397-6

988 Gao, X., and Wang, K. (2014). Strength of stick-slip and creeping subduction megathrusts
989 from heat flow observations. *Science*, *345*(6200), 1038-1041.
990 https://doi.org/10.1126/science.1255487

991 Gao, X., and Wang, K. (2017). Rheological separation of the megathrust seismogenic zone and
992 episodic tremor and slip. *Nature*, *543*(7645), 416-419. https://doi.org/10.1038/nature21389

993 Goldfinger, C., Nelson, C.H., Morey, A.E., Johnson, J.R., Patton, J., Karabanov, E.,
994 Gutierrez-Pastor, J., Eriksson, A.T., Gracia, E., Dunhill, G., Enkin, R.J., Dallimore, A., and
995 Vallier, T., 2012, Turbidite event history—Methods and implications for Holocene
996 paleoseismicity of the Cascadia subduction zone: U.S. Geological Survey Professional Paper
997 1661–F, 170 p, 64 figures, available at http://pubs.usgs.gov/pp/pp1661/f

998 Goldfinger, C., Galer, S., Beeson, J., Hamilton, T., Black, B., Romsos, C., Patton, J., Nelson,
999 C.H., Hausmann, R., & Morey, A. (2017). The importance of site selection, sediment supply,

1000 and hydrodynamics: A case study of submarine paleoseismology on the northern Cascadia
1001 margin, Washington USA. *Marine Geology*, *384*, 4-46.
1002 https://doi.org/10.1016/j.margeo.2016.06.008

1003 Guatteri, M., & Spudich, P. (2000). What can strong-motion data tell us about slip-weakening
1004 fault-friction laws?. *Bulletin of the Seismological Society of America*, *90*(1), 98-116.
1005 https://doi.org/10.1785/0119990053

1006 Han, S., Bangs, N. L., Carbotte, S. M., Saffer, D. M., and Gibson, J. C. (2017). Links between
1007 sediment consolidation and Cascadia megathrust slip behaviour. *Nature Geoscience*, *10*(12),
1008 954-959. https://doi.org/10.1038/s41561-017-0007-2

1009 Harris, R. A., Barall, M., Aagaard, B., Ma, S., Roten, D., Olsen, K., Duan, B., Liu, D., Luo, B.,
1010 Bai, K., Ampuero, J.P., Kaneko, Y., Gabriel, A.A., Duru, K., Ulrich, T., Wolherr, S., Shi, Z.,
1011 Durham, E., Bydlon, S., Zhang, Z., Chen, X., Somala, S.N., Pelties, C., Tago, J., Cruz-Atienza,
1012 V.M., Kozdon, J., Daub, E., Aslam, K., Kase, Y., Withers, K., and Dalguer, L. (2018). A suite
1013 of exercises for verifying dynamic earthquake rupture codes. *Seismological Research*
1014 *Letters*, *89*(3), 1146-1162. https://doi.org/10.1785/0220170222

1015 Ida, Y. (1972). Cohesive force across the tip of a longitudinal-shear crack and Griffith's
1016 specific surface energy. *Journal of Geophysical Research*, *77*(20), 3796-3805.
1017 https://doi.org/10.1029/JB077i020p03796

1018 Ide, S., & Aochi, H. (2013). Historical seismicity and dynamic rupture process of the 2011
1019 Tohoku-Oki earthquake. *Tectonophysics*, *600*, 1-13. https://doi.org/10.1016/j.tecto.2012.10.018

1020 Kelsey, H. M., Nelson, A. R., Hemphill-Haley, E., & Witter, R. C. (2005). Tsunami history of an
1021 Oregon coastal lake reveals a 4600 yr record of great earthquakes on the Cascadia subduction
1022 zone. *Geological Society of America Bulletin*, *117*(7-8), 1009-1032.
1023 https://doi.org/10.1130/B25452.1

1024 Lapusta, N., & Liu, Y. (2009). Three-dimensional boundary integral modeling of spontaneous
1025 earthquake sequences and aseismic slip. *Journal of Geophysical Research: Solid*
1026 *Earth*, *114*(B9). https://doi.org/10.1029/2008JB005934

1027 Li, D., & Liu, Y. (2021). Cascadia megathrust earthquake rupture model constrained by geodetic
1028 fault locking. *Philosophical Transactions of the Royal Society A*, *379*(2196), 20200135.
1029 https://doi.org/10.1098/rsta.2020.0135

1030 Li, S., Wang, K., Wang, Y., Jiang, Y., & Dosso, S. E. (2018). Geodetically inferred locking state
1031 of the Cascadia megathrust based on a viscoelastic Earth model [dataset]. *Journal of*
1032 *Geophysical Research: Solid Earth*, *123*(9), 8056-8072. https://doi.org/10.1029/2018JB015620

1033 Li, Y., Song, X., Shan, X., Qu, C., & Wang, Z. (2016). Locking degree and slip rate deficit
1034 distribution on MHT fault before 2015 Nepal Mw 7.9 earthquake. *Journal of Asian Earth*
1035 *Sciences*, *119*, 78-86. https://doi.org/10.1016/j.jseaes.2016.01.011

1036 Lindsey, E. O., Mallick, R., Hubbard, J. A., Bradley, K. E., Almeida, R. V., Moore, J. D.,
1037 Bürgmann, R., & Hill, E. M. (2021). Slip rate deficit and earthquake potential on shallow
1038 megathrusts [dataset]. *Nature Geoscience*, *14*(5), 321-326.
1039 https://doi.org/10.1038/s41561-021-00736-x

1040 Long, A. J., & Shennan, I. (1998). Models of rapid relative sea-level change in Washington and
1041 Oregon, USA. *The Holocene*, *8*(2), 129-142. https://doi.org/10.1191/095968398666306493

1042 Materna, K., Bartlow, N., Wech, A., Williams, C., and Bürgmann, R. (2019). Dynamically
1043 triggered changes of plate interface coupling in Southern Cascadia. *Geophysical Research*
1044 *Letters*, *46*(22), 12890-12899. https://doi.org/10.1029/2019GL084395

1045 McCaffrey, R., King, R. W., Payne, S. J., & Lancaster, M. (2013). Active tectonics of
1046 northwestern US inferred from GPS-derived surface velocities. *Journal of Geophysical*
1047 *Research: Solid Earth*, *118*(2), 709-723. https://doi.org/10.1029/2012JB009473

1048 McCrory, P. A., Blair, J. L., Oppenheimer, D. H., & Walter, S. R. (2004). Depth to the Juan de
1049 Fuca slab beneath the Cascadia subduction margin: A 3-D model for sorting earthquakes
1050 [dataset]. https://doi.org/10.3133/ds91

1051 Michel, S., Avouac, J. P., Lapusta, N., & Jiang, J. (2017). Pulse-like partial ruptures and high-
1052 frequency radiation at creeping-locked transition during megathrust earthquakes. *Geophysical*
1053 *Research Letters*, *44*(16), 8345-8351. https://doi.org/10.1002/2017GL074725

1054 Michel, S., Gualandi, A., and Avouac, J. P. (2019). Interseismic coupling and slow slip events on
1055 the Cascadia megathrust. *Pure and Applied Geophysics*, *176*(9), 3867-3891.
1056 https://doi.org/10.1007/s00024-018-1991-x

1057 Mikumo, T., Olsen, K. B., Fukuyama, E., & Yagi, Y. (2003). Stress-breakdown time and
1058 slip-weakening distance inferred from slip-velocity functions on earthquake faults. *Bulletin of*
1059 *the Seismological Society of America*, *93*(1), 264-282. https://doi.org/10.1785/0120020082

1060 Moreno, M., Rosenau, M., and Oncken, O. (2010). 2010 Maule earthquake slip correlates with
1061 pre-seismic locking of Andean subduction zone. *Nature*, *467*(7312), 198-202.
1062 https://doi.org/10.1038/nature09349

1063 Nur, A. (1978). Nonuniform friction as a physical basis for earthquake mechanics. *pure and*
1064 *applied geophysics*, *116*(4), 964-989. https://doi.org/10.1007/BF00876550

1065 Petersen, M.D., Moschetti, M.P., Powers, P.M., Mueller, C.S., Haller, K.M., Frankel, A.D.,
1066 Zeng, Yuehua, Rezaeian, Sanaz, Harmsen, S.C., Boyd, O.S., Field, Ned, Chen, Rui, Rukstales,
1067 K.S., Luco, Nico, Wheeler, R.L., Williams, R.A., and Olsen, A.H. (2014), Documentation for
1068 the 2014 update of the United States national seismic hazard maps: U.S. Geological Survey
1069 Open-File Report 2014–1091, 243 p., http://dx.doi.org/10.3133/ofr20141091

1070 Pollitz, F. F., & Evans, E. L. (2017). Implications of the earthquake cycle for inferring fault
1071 locking on the Cascadia megathrust. *Geophysical Journal International*, *209*(1), 167-185.
1072 https://doi.org/10.1093/gji/ggx009

1073 Priest, G. R., Goldfinger, C., Wang, K., Witter, R. C., Zhang, Y., & Baptista, A. M. (2009).
1074 Tsunami hazard assessment of the Northern Oregon coast: a multi-deterministic approach
1075 tested at Cannon Beach, Clatsop County, Oregon. *Oregon Department of Geology Mineral*
1076 *Industries Special Paper*, *41*, 87.

1077 Ramos, M. D., Huang, Y., Ulrich, T., Li, D., Gabriel, A. A., & Thomas, A. M. (2021). Assessing
1078 margin-wide rupture behaviors along the Cascadia megathrust with 3-D dynamic rupture
1079 simulations. *Journal of Geophysical Research: Solid Earth*, *126*(7), e2021JB022005.
1080 https://doi.org/10.1029/2021JB022005

1081 Rogers, G., & Dragert, H. (2003). Episodic tremor and slip on the Cascadia subduction zone:
1082 The chatter of silent slip. *science*, *300*(5627), 1942-1943.
1083 https://doi.org/10.1126/science.1084783

1084 Rowe, C. D., & Griffith, W. A. (2015). Do faults preserve a record of seismic slip: A second
1085 opinion. *Journal of Structural Geology*, *78*, 1-26. https://doi.org/10.1016/j.jsg.2015.06.006

1086 Saffer, D. M., & Tobin, H. J. (2011). Hydrogeology and mechanics of subduction zone
1087 forearcs: Fluid flow and pore pressure. *Annual Review of Earth and Planetary Sciences*, *39*,
1088 157-186. https://doi.org/10.1146/annurev-earth-040610-133408

1089 Satake, K., Wang, K., & Atwater, B. F. (2003). Fault slip and seismic moment of the 1700
1090 Cascadia earthquake inferred from Japanese tsunami descriptions. *Journal of Geophysical*
1091 *Research: Solid Earth*, *108*(B11). https://doi.org/10.1029/2003JB002521

1092 Schmalzle, G. M., McCaffrey, R., & Creager, K. C. (2014). Central Cascadia subduction zone
1093 creep [dataset]. *Geochemistry, Geophysics, Geosystems*, *15*(4), 1515-1532.
1094 https://doi.org/10.1002/2013GC005172

1095 Stanislowski, K., Roesner, A., and Ikari, M. J. (2022). Implications for megathrust slip
1096 behavior and pore pressure at the shallow northern Cascadia subduction zone from laboratory
1097 friction experiments. *Earth and Planetary Science Letters*, *578*, 117297.
1098 https://doi.org/10.1016/j.epsl.2021.117297

1099 Stephenson, W. J., Reitman, N. G., & Angster, S. J. (2017). *P-and S-wave velocity models*
1100 *incorporating the Cascadia subduction zone for 3D earthquake ground motion simulations,*
1101 *Version 1.6—Update for Open-File Report 2007–1348* (No. 2017-1152). US Geological Survey.
1102 https://doi.org/10.3133/ofr20171152

1103 Tinti, E., Fukuyama, E., Piatanesi, A., & Cocco, M. (2005). A kinematic source-time function
1104 compatible with earthquake dynamics. *Bulletin of the Seismological Society of America*, *95*(4),
1105 1211-1223. https://doi.org/10.1785/0120040177

1106 Tréhu, A. M., Blakely, R. J., & Williams, M. C. (2012). Subducted seamounts and recent
1107 earthquakes beneath the central Cascadia forearc. *Geology*, *40*(2), 103-106.
1108 https://doi.org/10.1130/G32460.1

1109 Ulrich, T., Gabriel, A. A., & Madden, E. H. (2022). Stress, rigidity and sediment strength
1110 control megathrust earthquake and tsunami dynamics. *Nature Geoscience*, 1-7.
1111 https://doi.org/10.1038/s41561-021-00863-5

1112 Walton, M.A., Staisch, L.M., Dura, T., Pearl, J.K., Sherrod, B., Gomberg, J., Engelhart, S.,
1113 Tréhu, A., Watt, J., Perkins, J., Witter, R.C., Bartlow, N., Goldfinger, C., Kelsey, H., Morey,
1114 A.E., Sahakian, V.J., Tobin, H., Wang, K., Wells, R., & Wirth, E. (2021). Toward an
1115 Integrative Geological and Geophysical View of Cascadia Subduction Zone Earthquakes.
1116 *Annual Review of Earth and Planetary Sciences*, *49*, 367-398.
1117 https://doi.org/10.1146/annurev-earth-071620-065605

1118 Wang, K., Wells, R., Mazzotti, S., Hyndman, R. D., & Sagiya, T. (2003). A revised dislocation
1119 model of interseismic deformation of the Cascadia subduction zone. *Journal of Geophysical*
1120 *Research: Solid Earth*, *108*(B1). https://doi.org/10.1029/2001JB001227

1121 Wang, K., & Dixon, T. (2004). "Coupling" semantics and science in earthquake research. *Eos,*
1122 *Transactions American Geophysical Union*, *85*(18), 180-180.
1123 https://doi.org/10.1029/2004EO180005

1124 Wang, K. (2007). 17. Elastic and Viscoelastic Models of Crustal Deformation in Subduction
1125 Earthquake Cycles. In *The seismogenic zone of subduction thrust faults* (pp. 540-575).
1126 Columbia University Press. https://doi.org/10.7312/dixo13866-017

1127 Wang, K., Hu, Y., & He, J. (2012). Deformation cycles of subduction earthquakes in a
1128 viscoelastic Earth. *Nature*, *484*(7394), 327-332. https://doi.org/10.1038/nature11032

1129 Wang, K., & Tréhu, A. M. (2016). Invited review paper: Some outstanding issues in the study
1130 of great megathrust earthquakes—The Cascadia example. *Journal of Geodynamics*, *98*, 1-18.
1131 https://doi.org/10.1016/j.jog.2016.03.010

1132 Wang, P. L., Engelhart, S. E., Wang, K., Hawkes, A. D., Horton, B. P., Nelson, A. R., & Witter,
1133 R. C. (2013). Heterogeneous rupture in the great Cascadia earthquake of 1700 inferred from
1134 coastal subsidence estimates. *Journal of Geophysical Research: Solid Earth*, *118*(5),
1135 2460-2473. https://doi.org/10.1002/jgrb.50101

1136 Watt, J. T., & Brothers, D. S. (2021). Systematic characterization of morphotectonic variability
1137 along the Cascadia convergent margin: Implications for shallow megathrust behavior and
1138 tsunami hazards. *Geosphere*, *17*(1), 95-117. https://doi.org/10.1130/GES02178.1

1139 Wells, D. L., & Coppersmith, K. J. (1994). New empirical relationships among magnitude,
1140 rupture length, rupture width, rupture area, and surface displacement. *Bulletin of the*
1141 *seismological Society of America*, *84*(4), 974-1002. https://doi.org/10.1785/BSSA0840040974

1142 Weng, H., & Ampuero, J. P. (2020). Continuum of earthquake rupture speeds enabled by
1143 oblique slip. *Nature Geoscience*, *13*(12), 817-821. https://doi.org/10.1038/s41561-020-00654-4

1144 Weng, H., & Yang, H. (2018). Constraining frictional properties on fault by dynamic rupture
1145 simulations and near-field observations. *Journal of Geophysical Research: Solid Earth*, *123*(8),
1146 6658-6670. https://doi.org/10.1029/2017JB015414

1147 Wilson, A., & Ma, S. (2021). Wedge plasticity and fully coupled simulations of dynamic
1148 rupture and tsunami in the Cascadia subduction zone. *Journal of Geophysical Research: Solid*
1149 *Earth*, *126*(7), e2020JB021627. https://doi.org/10.1029/2020JB021627

1150 Witter, R. C., Zhang, Y., Wang, K., Goldfinger, C., Priest, G. R., & Allan, J. C. (2012).
1151 Coseismic slip on the southern Cascadia megathrust implied by tsunami deposits in an Oregon
1152 lake and earthquake-triggered marine turbidites. *Journal of Geophysical Research: Solid*
1153 *Earth*, *117*(B10). https://doi.org/10.1029/2012JB009404

1154 Yang, H., Yao, S., He, B., Newman, A. V., & Weng, H. (2019a). Deriving rupture scenarios
1155 from interseismic locking distributions along the subduction megathrust. *Journal of*
1156 *Geophysical Research: Solid Earth*, *124*(10), 10376-10392.
1157 https://doi.org/10.1029/2019JB017541

1158 Yang, H., Yao, S., He, B., & Newman, A. V. (2019b). Earthquake rupture dependence on
1159 hypocentral location along the Nicoya Peninsula subduction megathrust. *Earth and Planetary*
1160 *Science Letters*, *520*, 10-17. https://doi.org/10.1016/j.epsl.2019.05.030

1161 Yao, S., & Yang, H. (2020). Rupture dynamics of the 2012 Nicoya Mw 7.6 earthquake:
1162 Evidence for low strength on the megathrust. *Geophysical Research Letters*, *47*(13),
1163 e2020GL087508. https://doi.org/10.1029/2020GL087508

1164 Yao, S., & Yang, H. (2022). Hypocentral dependent shallow slip distribution and rupture
1165 extents along a strike-slip fault. *Earth and Planetary Science Letters*, *578*, 117296.
1166 https://doi.org/10.1016/j.epsl.2021.117296